Gravity driven free surface flow of granular avalanches over complex topography

3 authors, including:

J. M. N. T. Gray
The University of Manchester
129 PUBLICATIONS **6,027** CITATIONS

Columban Hutter
ETH Zurich
461 PUBLICATIONS **14,579** CITATIONS

Gravity-driven free surface flow of granular avalanches over complex basal topography

By J. M. N. T. Gray†, M. Wieland and K. Hutter

*Institut für Mechanik, Technische Universität Darmstadt,
64289 Darmstadt, Germany*

A two-dimensional depth-integrated theory is derived for the gravity-driven free surface flow of cohesionless granular avalanches over complex shallow basal topography. This is an important extension of the one-dimensional Savage–Hutter theory. A simple curvilinear coordinate system is adopted, which is fitted to the 'mean' downslope chute topography. This defines a quasi-two-dimensional *reference* surface on top of which shallow three-dimensional basal topography is superposed. The governing equations are expressed in the curvilinear coordinate system and the mass- and momentum-balance equations are integrated through the avalanche depth. An ordering argument and a Mohr–Coulomb closure model are used to obtain a simple reduced system of equations. Laboratory experiments have been performed on a partly confined chute to validate the theory. An avalanche is released on a section inclined at 40° to the horizontal, on which there is a concave parabolic cross-slope profile, and runs out through a smooth transition zone onto a horizontal plane. A comparison of the experiment with numerical solutions shows that the avalanche tail speed is under-predicted. A modification to the bed-friction angle is proposed, which brings theory and experiment into very good agreement. The partly confined chute channels the flow and results in significantly longer maximum run-out distances than on an unconfined chute. A simple shallow-water avalanche model is also derived and tested against the experimental results.

Keywords: avalanches; rapid granular flow; depth-integrated equations;
Mohr–Coulomb behaviour; gravity flow; hyperbolic equations

1. Introduction

Granular avalanches are abundant in the natural environment on a very wide range of length-scales and occur when a layer of granular material becomes unstable. In the geophysical context, rock-falls, landslides and snow-slab avalanches may set up to $10^{10}\,\mathrm{m}^3$ of material in motion, while in industrial flows in silos, hoppers, rotating drums or on slag heaps the volume of material is of the order of several cubic centimetres to several hundreds of cubic metres. Despite the enormous difference in length-scales the dominant physical mechanisms that drive the flow are similar.

The first continuum theory to describe the motion of shallow avalanches was developed by Savage & Hutter (1989). The granular avalanche was assumed to be a shallow

---

† Address from November 1999: Department of Mathematics, University of Manchester, Manchester M13 9PL, UK.

incompressible Mohr–Coulomb material that slid down a rigid surface. The leading-order plane two-dimensional equations were integrated through the avalanche depth to obtain a spatially one-dimensional theory for the flow down a slope of constant inclination angle ζ_0.

In many situations a complete knowledge of the avalanche motion is required from initiation, on a steep slope, to run-out on a shallow slope. A simple curvilinear coordinate system was introduced by Savage & Hutter (1991), which allowed such flows to be modelled. The coordinates were generated by the local normal and tangent vectors to the rigid basal surface. These acted as spatially variable basis vectors, which allowed the local inclination angle ζ to change as a function of the downslope coordinate x. Laboratory experiments on an exponentially curved chute (Hutter & Koch 1991) and on concave and convex chutes (Greve & Hutter 1993; Hutter *et al.* 1995) demonstrated extremely good agreement with predictions from this theory.

The theory has also been generalized to three dimensions by Hutter *et al.* (1993) and Greve *et al.* (1994) to model the unconfined flow of granular materials. Hutter *et al.* (1993) derived the leading-order equations for motion on a plane of mean inclination angle ζ_0, while Greve *et al.* (1994) added a lateral y-coordinate, orthogonal to the curvilinear coordinates of Savage & Hutter (1991), which allowed the flow of avalanches to be computed on three-dimensional topography with no lateral curvature. Good agreement was obtained between theoretical predictions and laboratory experiments (Koch *et al.* 1994).

In this paper the Savage–Hutter theory is extended to model the flow of avalanches over complex three-dimensional topography and the model is tested against a laboratory experiment. The model is able to predict the flow over realistic topographic features and provide site-specific information about the maximum run-out distance. This is of importance to civil engineers who must decide where further development in populated mountainous regions is safe.

2. Governing equations

The avalanche is assumed to be an incompressible material with constant density ρ_0 throughout the entire body. It follows that the fundamental point differential form of the mass and momentum conservation laws reduce to

$$\nabla \cdot \boldsymbol{u} = 0, \tag{2.1}$$

$$\rho_0 \left\{ \frac{\partial \boldsymbol{u}}{\partial t} + \nabla \cdot (\boldsymbol{u} \otimes \boldsymbol{u}) \right\} = -\nabla \cdot \boldsymbol{p} + \rho_0 \boldsymbol{g}, \tag{2.2}$$

where $\boldsymbol{u}$ is the velocity, $\otimes$ is the tensor (or dyadic) product, $\boldsymbol{p}$ is the pressure tensor (the negative Cauchy stress) and $\boldsymbol{g}$ is the gravitational acceleration. The momentum balance is usually presented in a reduced form in which the mass balance (2.1) and the tensor relation $\nabla \cdot (\boldsymbol{u} \otimes \boldsymbol{u}) = \boldsymbol{u}(\nabla \cdot \boldsymbol{u}) + (\nabla \boldsymbol{u})\boldsymbol{u}$ are used to simplify the left-hand side of (2.2). Here it is left in its fundamental point form, as this makes the transformation into curvilinear coordinates and the process of integration through the avalanche depth considerably easier.

The granular avalanche is assumed to satisfy a Mohr–Coulomb yield criterion (Savage & Hutter 1989) in which the internal shear stress $\boldsymbol{S}$ and the normal pressure N on any plane element are related by

$$|\boldsymbol{S}| = N \tan \phi, \tag{2.3}$$

where ϕ is the internal angle of friction.

The conservation laws (2.1) and (2.2) are subject to kinematic boundary conditions at the free surface, $F^{\mathrm{s}}(\boldsymbol{x}, t) = 0$, and at the base, $F^{\mathrm{b}}(\boldsymbol{x}, t) = 0$, of the avalanche

$$F^{\mathrm{s}}(\boldsymbol{x}, t) = 0, \quad \frac{\partial F^{\mathrm{s}}}{\partial t} + \boldsymbol{u}^{\mathrm{s}} \cdot \nabla F^{\mathrm{s}} = 0, \tag{2.4}$$

$$F^{\mathrm{b}}(\boldsymbol{x}, t) = 0, \quad \frac{\partial F^{\mathrm{b}}}{\partial t} + \boldsymbol{u}^{\mathrm{b}} \cdot \nabla F^{\mathrm{b}} = 0, \tag{2.5}$$

where the superscripts 's' and 'b' indicate that a variable is evaluated at the surface and base, respectively. Note that in most situations of practical interest the basal geometry of the avalanche is determined by the fixed topography it is sliding over and $\partial F^{\mathrm{b}}/\partial t = 0$.

The free surface of the avalanche is traction free while the base satisfies a Coulomb dry-friction sliding law. That is,

$$F^{\mathrm{s}}(\boldsymbol{x}, t) = 0, \quad \boldsymbol{p}^{\mathrm{s}} \boldsymbol{n}^{\mathrm{s}} = \boldsymbol{0}, \tag{2.6}$$

$$F^{\mathrm{b}}(\boldsymbol{x}, t) = 0, \quad \boldsymbol{p}^{\mathrm{b}} \boldsymbol{n}^{\mathrm{b}} - \boldsymbol{n}^{\mathrm{b}}(\boldsymbol{n}^{\mathrm{b}} \cdot \boldsymbol{p}^{\mathrm{b}} \boldsymbol{n}^{\mathrm{b}}) = (\boldsymbol{u}^{\mathrm{b}}/|\boldsymbol{u}^{\mathrm{b}}|) \tan \delta (\boldsymbol{n}^{\mathrm{b}} \cdot \boldsymbol{p}^{\mathrm{b}} \boldsymbol{n}^{\mathrm{b}}), \tag{2.7}$$

where the surface and basal normals are

$$\boldsymbol{n}^{\mathrm{s}} = \frac{\nabla F_{\mathrm{s}}}{|\nabla F_{\mathrm{s}}|}, \quad \boldsymbol{n}^{\mathrm{b}} = \frac{\nabla F_{\mathrm{b}}}{|\nabla F_{\mathrm{b}}|}. \tag{2.8}$$

Note that $\boldsymbol{p}\boldsymbol{n}$ is the negative traction vector, $\boldsymbol{n} \cdot \boldsymbol{p}\boldsymbol{n}$ is the normal pressure and $\boldsymbol{p}\boldsymbol{n} - \boldsymbol{n}(\boldsymbol{n} \cdot \boldsymbol{p}\boldsymbol{n})$ is the negative shear traction. It follows that the Coulomb dry-friction law (2.7) expresses the fact that the magnitude of the basal shear stress equals the normal basal pressure multiplied by a coefficient of friction $\tan \delta$. The function δ is termed the basal angle of friction. The shear traction is assumed to point in the opposite direction to the basal velocity $\boldsymbol{u}^{\mathrm{b}}$ in (2.7). Note that this implicitly assumes that the basal topography is fixed, so that $\boldsymbol{u}^{\mathrm{b}} \cdot \boldsymbol{n}^{\mathrm{b}} = 0$ by (2.5) and hence that the basal velocity $\boldsymbol{u}^{\mathrm{b}}$ is tangential to the basal surface. Defining the direction of the shear stress in this way introduces a singularity into the equations at $\boldsymbol{u}^{\mathrm{b}} = \boldsymbol{0}$, which restricts the theory to problems in which the basal velocity retains the same sign throughout its motion. For practical modelling of landslides, rock falls and snow avalanches this restriction only presents problems near the end of the avalanche motion, when it seeks to come to rest.

3. Curvilinear coordinates

The complex basal topography is modelled by defining an orthogonal curvilinear *reference* surface, such as in figure 1, and then superposing shallow basal topography on it, as shown in figure 2. The reference surface is not uniquely defined and various choices are possible. For instance, it could follow the 'mean' downslope topography or be fitted to a single cross-section of the specified geometry. However, the superposed topography must be shallow with respect to the reference surface, which places some restrictions on the permissible geometry.

To make this precise a rectangular Cartesian coordinate system $O'XYZ$ is defined with unit basis vectors $\boldsymbol{i}, \boldsymbol{j}, \boldsymbol{k}$ aligned so that the unit vector $\boldsymbol{k}$ is parallel, but in the opposite sense, to the gravity acceleration vector and $\boldsymbol{i}$ lies in the vertical plane in which the reference surface varies. A simple curvilinear coordinate system $Oxyz$ is
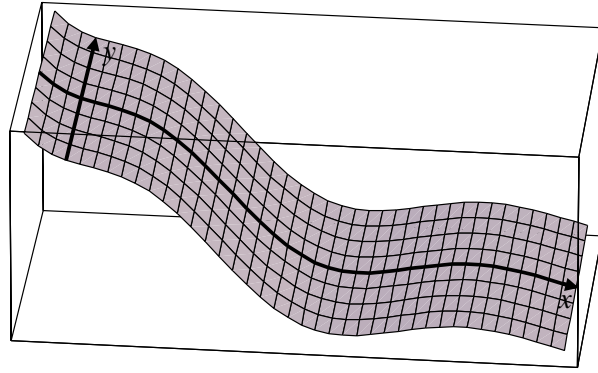
Figure 1. A simple orthogonal coordinate system is defined by a quasi-two-dimensional *reference surface*, an example of which is illustrated here. The surface has no cross-slope variation in curvature, that is, there is no lateral variation of the reference topography in the y-direction, but the downslope inclination angle (to the horizontal), ζ, changes as a function of the downslope coordinate x. The z coordinate is defined as the local normal to the reference surface.
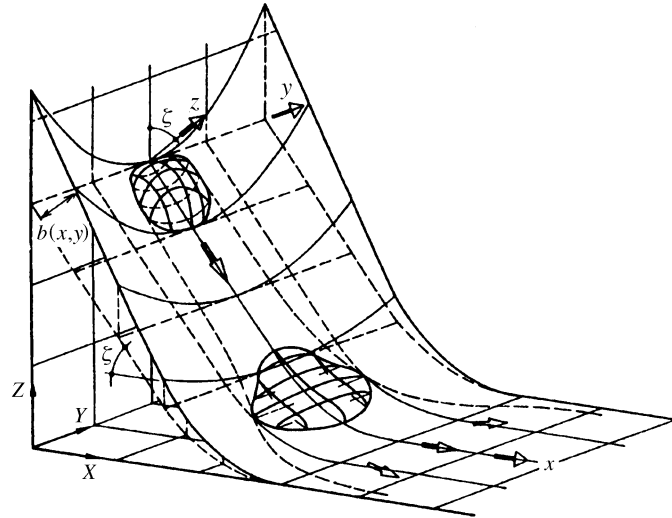

Figure 2. The rectangular Cartesian coordinate system $O'XYZ$ is aligned so that the Z-axis is parallel but opposite in direction to the gravity acceleration vector, and the Y-axis is parallel to the cross-slope reference surface coordinate y. The basal topography (solid lines) on which the avalanche slides, $F^{\mathrm{b}}(\boldsymbol{x}) = 0$, is defined by its height above the curvilinear reference surface $F^{\mathrm{b}} = b(x, y) - z$ (dashed lines). The shallow complex three-dimensional geometry is therefore superposed on the quasi-two-dimensional reference surface.

introduced following Greve *et al.* (1994), which is similar to that of Savage & Hutter (1991). In these coordinates the position vector of a point $\boldsymbol{r}$ is given by

$$\boldsymbol{r} = \boldsymbol{r}^{\mathrm{r}}(x, y) + z\boldsymbol{n}^{\mathrm{r}}, \tag{3.1}$$

where $\boldsymbol{r}^{\mathrm{r}}$ is the position vector of the reference surface and $\boldsymbol{n}^{\mathrm{r}}$ is normal to the reference surface. In Cartesian coordinates the normal to the reference surface is

given by

$$\boldsymbol{n}^{\mathrm{r}} = \sin \zeta \boldsymbol{i} + \cos \zeta \boldsymbol{k}, \tag{3.2}$$

where ζ is the inclination angle of the normal relative to the Z-axis. For ease of notation the identification that $(x, y, z) = (x^1, x^2, x^3)$ is made. These are the contravariant components in the curvilinear coordinate system (Sokolnikoff 1951; McConnell 1957; Brillouin 1964; Klingbeil 1966) and the associated covariant basis vectors, $\boldsymbol{g}_i$, are given by (see, for example, Klingbeil 1966)

$$\boldsymbol{g}_i = \frac{\partial \boldsymbol{r}}{\partial x^i} = \boldsymbol{r}_{,i}, \tag{3.3}$$

where the $(\ )_{,i}$ notation is used to indicate contravariant differentiation. In evaluating the covariant basis vectors of the curvilinear coordinate system (3.1), the gradients $\partial \boldsymbol{r}^{\mathrm{r}}/\partial x^1$ and $\partial \boldsymbol{r}^{\mathrm{r}}/\partial x^2$ arise. These are simply the tangent vectors to the reference surface in the x^1- and x^2-directions, respectively. Thus, choosing orthogonal tangent vectors with the x-axis in the $O'XZ$ plane it follows that $\partial \boldsymbol{r}^{\mathrm{r}}/\partial x^1 = \cos \zeta \boldsymbol{i} - \sin \zeta \boldsymbol{k}$ and $\partial \boldsymbol{r}^{\mathrm{r}}/\partial x^2 = \boldsymbol{j}$, so that

$$\left.\begin{aligned} \boldsymbol{g}_1 &= (1 - \kappa x^3)(\cos \zeta \boldsymbol{i} - \sin \zeta \boldsymbol{k}), \\ \boldsymbol{g}_2 &= \boldsymbol{j}, \\ \boldsymbol{g}_3 &= \sin \zeta \boldsymbol{i} + \cos \zeta \boldsymbol{k}, \end{aligned}\right\} \tag{3.4}$$

where the curvature

$$\kappa = -\frac{\partial \zeta}{\partial x^1}. \tag{3.5}$$

The covariant metric coefficients are defined as $g_{ij} = \boldsymbol{g}_i \cdot \boldsymbol{g}_j$ (see, for example, Klingbeil 1966) and it follows from (3.4) that

$$(g_{ij}) = \begin{pmatrix} (1 - \kappa x^3)^2 & 0 & 0 \\ 0 & 1 & 0 \\ 0 & 0 & 1 \end{pmatrix}. \tag{3.6}$$

The off-diagonal elements of the metric tensor are zero, which implies that these simple curvilinear coordinates are orthogonal. Note that these coordinates possess a singularity at all points where $x^3 = 1/\kappa$. Physically, these points correspond to the positions at which consecutive z-axes (which vary locally) intersect with one another. Provided the avalanche does not pass through one of these points during the course of its motion the curvilinear coordinates (3.6) represent a valid coordinate system.

The covariant unit vectors are defined as $\boldsymbol{g}_i^* = \boldsymbol{g}_i/\sqrt{g_{(ii)}}$, where the Einstein summation convention is dropped for the bracketed indices, i.e. $\boldsymbol{g}_1^* = \cos \zeta \boldsymbol{i} - \sin \zeta \boldsymbol{k}$, $\boldsymbol{g}_2^* = \boldsymbol{j}$ and $\boldsymbol{g}_3^* = \sin \zeta \boldsymbol{i} + \cos \zeta \boldsymbol{k}$. The contravariant basis vectors $\boldsymbol{g}^j$, which are distinguished by the superscript indices, are constructed by

$$\boldsymbol{g}_i \cdot \boldsymbol{g}^j = \delta_i^j = \begin{cases} 1, & i = j, \\ 0, & i \neq j. \end{cases} \tag{3.7}$$

That is, $\boldsymbol{g}^1 = (\cos \zeta \boldsymbol{i} - \sin \zeta \boldsymbol{k})/(1 - \kappa x^3)$, $\boldsymbol{g}^2 = \boldsymbol{j}$ and $\boldsymbol{g}^3 = \sin \zeta \boldsymbol{i} + \cos \zeta \boldsymbol{k}$. The associated contravariant metric coefficients are $g^{(11)} = 1/(1 - \kappa x^3)^2$, $g^{(22)} = 1$, $g^{(33)} = 1$ and the off-diagonal elements are equal to zero.

In contrast to the unit vectors $\boldsymbol{i}$, $\boldsymbol{j}$ and $\boldsymbol{k}$, the covariant vectors $\boldsymbol{g}_i$ vary as functions of position. As a consequence, gradients of tensor quantities give rise to extra terms associated with the spatial variation of the curvilinear vectors. In particular the gradient

$$\boldsymbol{g}_{k,l} = \Gamma_{kl}^j \boldsymbol{g}_j, \tag{3.8}$$

where the Christoffel symbol in orthogonal curvilinear coordinates is (see, for example, Klingbeil 1966)

$$\Gamma_{lm}^k = \tfrac{1}{2} g^{(kk)} (g_{mk,l} + g_{kl,m} - g_{lm,k}), \tag{3.9}$$

and the Einstein convention is again dropped for the bracketed indices. For the curvilinear coordinate system (3.6) the components of the Christoffel symbol are given by

$$\boldsymbol{\Gamma}^1 = \frac{-1}{1 - \kappa z} \begin{pmatrix} \kappa' z & 0 & \kappa \\ 0 & 0 & 0 \\ \kappa & 0 & 0 \end{pmatrix}, \quad \boldsymbol{\Gamma}^2 = \boldsymbol{0}, \quad \boldsymbol{\Gamma}^3 = (1 - \kappa z) \begin{pmatrix} \kappa & 0 & 0 \\ 0 & 0 & 0 \\ 0 & 0 & 0 \end{pmatrix}, \tag{3.10}$$

where $\kappa' = \partial \kappa / \partial x^1$.

The conservation laws and their associated boundary conditions were given in coordinate independent form in §2. In order to express these results in curvilinear coordinates, three key results are required, namely the gradient of a scalar field, the divergence of a vector field and the divergence of a tensor field. All these results can easily be derived by using the ∇-vector, which is defined as

$$\nabla = \boldsymbol{g}^k \frac{\partial}{\partial x^k}, \tag{3.11}$$

with components given in terms of the contravariant basis $\boldsymbol{g}^k$. The gradient of a scalar field F is $\nabla F = F_{,k} \boldsymbol{g}^k$. This is expressed in terms of the covariant unit base vectors

$$\nabla F = \frac{\partial F}{\partial x^k} g^{(kk)} \sqrt{g_{(kk)}} \boldsymbol{g}_k^*, \tag{3.12}$$

which reduces to

$$\nabla F = \frac{1}{1 - \kappa z} \frac{\partial F}{\partial x} \boldsymbol{g}_1^* + \frac{\partial F}{\partial y} \boldsymbol{g}_2^* + \frac{\partial F}{\partial z} \boldsymbol{g}_3^* \tag{3.13}$$

for the simple curvilinear coordinate system defined in (3.6). Note that the final result is written in terms of the variables (x, y, z) instead of the equivalent form (x^1, x^2, x^3).

Given a vector field $\boldsymbol{u} = u^i \boldsymbol{g}_i$, its divergence is

$$\nabla \cdot \boldsymbol{u} = \left(\boldsymbol{g}^k \frac{\partial}{\partial x^k} \right) \cdot (u_i \boldsymbol{g}_i) = u_{,i}^i + u^i \Gamma_{ik}^k. \tag{3.14}$$

The vector's physical components u^{i*} (defined relative to unit base vectors) are related to the contravariant components by $u^i = u^{i*} / \sqrt{g_{(ii)}}$. Substituting these into (3.14) together with the Christoffel symbols (3.9) implies that the divergence of a vector $\boldsymbol{u}$ in curvilinear coordinates is

$$\nabla \cdot \boldsymbol{u} = \frac{\partial}{\partial x} \left(\frac{u^{1*}}{1 - \kappa z} \right) + \frac{\partial u^{2*}}{\partial y} + \frac{\partial u^{3*}}{\partial z} - \frac{u^{1*} \kappa' z}{(1 - \kappa z)^2} - \frac{u^{3*} \kappa}{1 - \kappa z}. \tag{3.15}$$

Similarly, given a symmetric second-order tensor $\boldsymbol{p} = p^{ij}\boldsymbol{g}_i\boldsymbol{g}_j$, the divergence

$$\nabla \cdot \boldsymbol{p} = \left(\boldsymbol{g}^k \frac{\partial}{\partial x^k}\right) \cdot (p^{ij}\boldsymbol{g}_i\boldsymbol{g}_j) = \{p^{ki}_{,k} + p^{ji}\Gamma^k_{jk} + p^{kj}\Gamma^i_{jk}\}\sqrt{g_{(ii)}}\boldsymbol{g}^*_i. \tag{3.16}$$

The physical components p^{ij*} of a second-order tensor are related to the contravariant components by $p^{ij} = p^{ij*}/(\sqrt{g_{(ii)}}\sqrt{g_{(jj)}})$. Substituting this in (3.16) together with the Christoffel symbols (3.9) implies that the curvilinear form of the divergence of a symmetric tensor $\boldsymbol{p}$ is

$$\begin{aligned}
\nabla \cdot \boldsymbol{p} =& \left(\frac{\partial}{\partial x}\left(\frac{p^{11*}}{1-\kappa z}\right) + \frac{\partial p^{12*}}{\partial y} + \frac{\partial p^{13*}}{\partial z} - \frac{\kappa' z p^{11*}}{(1-\kappa z)^2} - \frac{2\kappa p^{13*}}{1-\kappa z}\right)\boldsymbol{g}^*_1 \\
&+ \left(\frac{\partial}{\partial x}\left(\frac{p^{12*}}{1-\kappa z}\right) + \frac{\partial p^{22*}}{\partial y} + \frac{\partial p^{23*}}{\partial z} - \frac{\kappa' z p^{12*}}{(1-\kappa z)^2} - \frac{\kappa p^{23*}}{1-\kappa z}\right)\boldsymbol{g}^*_2 \\
&+ \left(\frac{\partial}{\partial x}\left(\frac{p^{13*}}{1-\kappa z}\right) + \frac{\partial p^{23*}}{\partial y} + \frac{\partial p^{33*}}{\partial z} - \frac{\kappa' z p^{13*}}{(1-\kappa z)^2} - \frac{\kappa(p^{33*} - p^{11*})}{1-\kappa z}\right)\boldsymbol{g}^*_3.
\end{aligned} \tag{3.17}$$

Note that the transformations for the divergence of vector and tensor quantities given in (3.15) and (3.17), respectively, can be simplified, but they are left in the given form as this proves to be particularly useful when the free surface and basal boundary conditions are included during the depth-integration process in § 5.

4. Non-dimensional equations

In this section the coordinate independent equations of § 2 are expressed in terms of the simple curvilinear coordinate system introduced in § 3. A set of scalings that reflect the dominant balances is also introduced in order to non-dimensionalize the equations, but all results presented in this section are exact.

For notational consistency with Hutter *et al.* (1993) and Greve *et al.* (1994) the physical components of the velocity field $\boldsymbol{u}$ are defined as u, v and w in the downslope, cross-slope and normal directions to the reference surface, respectively. Similarly, the physical components of the symmetric pressure tensor $\boldsymbol{p}$ are $p_{xx}, p_{yy}, p_{zz}, p_{xy}, p_{xz}, p_{yz}$, where the convention that subscripts define covariant quantities is now dropped. Following Savage & Hutter (1989), the physical variables are non-dimensionalized using the scalings

$$\left.\begin{aligned}
(x, y, z, F^{\mathrm{s}}, F^{\mathrm{b}}, t) &= (L\hat{x}, L\hat{y}, H\hat{z}, H\hat{F}^{\mathrm{s}}, H\hat{F}^{\mathrm{b}}, (L/g)^{1/2}\hat{t}), \\
(u, v, w) &= (gL)^{1/2}(\hat{u}, \hat{v}, \varepsilon\hat{w}), \\
(p_{xx}, p_{yy}, p_{zz}) &= \rho_0 g H(\hat{p}_{xx}, \hat{p}_{yy}, \hat{p}_{zz}), \\
(p_{xy}, p_{xz}, p_{yz}) &= \rho_0 g H \mu(\hat{p}_{xy}, \hat{p}_{xz}, \hat{p}_{yz}), \\
\kappa &= \hat{\kappa}/\mathcal{R},
\end{aligned}\right\} \tag{4.1}$$

where the hats represent non-dimensional variables. The scalings (4.1) assume that the avalanche has a typical length-scale L tangential to the reference surface and a typical thickness H normal to it. Furthermore, a balance between the downslope acceleration, $\partial u/\partial t$, the downslope advection, $u\partial u/\partial x$, and the gravitational acceleration (in the downslope momentum balance) implies that typical downslope velocity magnitudes are of order $(gL)^{1/2}$ and that the time-scale for order-unity changes is

$(L/g)^{1/2}$. Velocities normal to the slope are of order $(H/L)(gL)^{1/2}$ by mass balance. Furthermore, assuming a granular static balance, typical normal pressures at the base of the avalanche are of order $\rho_0 gH$, and the Coulomb dry-friction law suggests that the basal shear stresses are of order $\rho_0 gH \tan \delta_0$, where δ_0 is a typical basal angle of friction. Finally, the downslope curvature of the reference surface, κ, is assumed to be of order $1/\mathcal{R}$. These scalings introduce three non-dimensional parameters:

$$\varepsilon = H/L, \quad \lambda = L/\mathcal{R}, \quad \mu = \tan \delta_0, \tag{4.2}$$

where ε is the aspect ratio of the avalanche, λ is a measure of the curvature of the reference geometry with respect to the length of the avalanche and μ is a coefficient of friction. The size of these parameters plays a crucial role in the ordering arguments of §6.

The mass-balance equation (2.1) can be written in the curvilinear coordinates of §3 by using the transformation rule (3.14) for the divergence of a vector. Applying the scalings (4.1) it follows that the non-dimensional curvilinear form of the mass-balance equation is

$$\frac{\partial}{\partial x}(u\Psi) + \frac{\partial v}{\partial y} + \frac{\partial w}{\partial z} - \varepsilon\lambda\kappa' z u\Psi^2 - \varepsilon\lambda\kappa w\Psi = 0, \tag{4.3}$$

where the hats are now dropped, and

$$\Psi = \frac{1}{1 - \varepsilon\lambda\kappa z}. \tag{4.4}$$

The momentum-balance equation (2.2) can be written in curvilinear coordinates by using relation (3.17) to transform the tensor $\boldsymbol{u} \otimes \boldsymbol{u}$ and the pressure $\boldsymbol{p}$. It follows that the non-dimensional curvilinear components of the momentum balance in the downslope, cross-slope and normal directions to the reference surface are

$$\frac{\partial u}{\partial t} + \frac{\partial}{\partial x}(u^2\Psi) + \frac{\partial}{\partial y}(uv) + \frac{\partial}{\partial z}(uw) - \varepsilon\lambda\kappa' z u^2\Psi^2 - 2\varepsilon\lambda\kappa uw\Psi$$
$$= \sin\zeta - \varepsilon\mu\frac{\partial}{\partial x}(p_{xx}\Psi) - \varepsilon\mu\frac{\partial p_{xy}}{\partial y} - \mu\frac{\partial p_{xz}}{\partial z} + \varepsilon^2\lambda\kappa' z p_{xx}\Psi^2 + 2\varepsilon\lambda\mu\kappa p_{xz}\Psi, \tag{4.5}$$

$$\frac{\partial v}{\partial t} + \frac{\partial}{\partial x}(uv\Psi) + \frac{\partial}{\partial y}(v^2) + \frac{\partial}{\partial z}(vw) - \varepsilon\lambda\kappa' z uv\Psi^2 - \varepsilon\lambda\kappa vw\Psi$$
$$= -\varepsilon\mu\frac{\partial}{\partial x}(p_{xy}\Psi) - \varepsilon\frac{\partial p_{yy}}{\partial y} - \mu\frac{\partial p_{yz}}{\partial z} + \varepsilon^2\lambda\mu\kappa' z p_{xy}\Psi^2 + \varepsilon\lambda\mu\kappa p_{yz}\Psi, \tag{4.6}$$

$$\varepsilon\left\{\frac{\partial w}{\partial t} + \frac{\partial}{\partial x}(uw\Psi) + \frac{\partial}{\partial y}(vw) + \frac{\partial}{\partial z}(w^2)\right\} - \varepsilon^2\lambda\kappa' z\, uw\Psi^2 - \lambda\kappa(\varepsilon^2 w^2 - u^2)\Psi$$
$$= -\cos\zeta - \varepsilon\mu\frac{\partial}{\partial x}(p_{xz}\Psi) - \varepsilon\mu\frac{\partial p_{yz}}{\partial y} - \frac{\partial p_{zz}}{\partial z} + \varepsilon^2\lambda\mu\kappa' z p_{xz}\Psi^2 + \varepsilon\lambda\kappa(p_{zz} - p_{xx})\Psi, \tag{4.7}$$

respectively. The free surface of the avalanche, F^{s}, and basal topography over which the avalanche is assumed to slide, F^{b}, are defined by their respective heights above the curvilinear reference surface:

$$F^{\mathrm{s}} = z - s(x, y, t) = 0, \quad F^{\mathrm{b}} = b(x, y, t) - z = 0. \tag{4.8}$$

Using (3.13) and (4.1) it follows that the non-dimensional curvilinear form of the surface and basal kinematic conditions (2.4) and (2.5) are

$$z = s(x, y, t), \quad \frac{\partial s}{\partial t} + u^{\mathrm{s}}\Psi^{\mathrm{s}}\frac{\partial s}{\partial x} + v^{\mathrm{s}}\frac{\partial s}{\partial y} - w^{\mathrm{s}} = 0, \tag{4.9}$$

$$z = b(x, y, t), \quad \frac{\partial b}{\partial t} + u^{\mathrm{b}}\Psi^{\mathrm{b}}\frac{\partial b}{\partial x} + v^{\mathrm{b}}\frac{\partial b}{\partial y} - w^{\mathrm{b}} = 0. \tag{4.10}$$

Similarly, the traction free boundary condition at the free surface of the avalanche (2.6) has downslope, cross-slope and normal components

$$\left. \begin{aligned} -\varepsilon p_{xx}^{\mathrm{s}}\Psi^{\mathrm{s}}\frac{\partial s}{\partial x} - \varepsilon\mu p_{xy}^{\mathrm{s}}\frac{\partial s}{\partial y} + \mu p_{xz}^{\mathrm{s}} = 0, \\ -\varepsilon\mu p_{yx}^{\mathrm{s}}\Psi^{\mathrm{s}}\frac{\partial s}{\partial x} - \varepsilon p_{yy}^{\mathrm{s}}\frac{\partial s}{\partial y} + \mu p_{yz}^{\mathrm{s}} = 0, \\ -\varepsilon\mu p_{zx}^{\mathrm{s}}\Psi^{\mathrm{s}}\frac{\partial s}{\partial x} - \varepsilon\mu p_{zy}^{\mathrm{s}}\frac{\partial s}{\partial y} + p_{zz}^{\mathrm{s}} = 0, \end{aligned} \right\} \tag{4.11}$$

respectively. The Coulomb basal sliding law (2.7) implies that the negative basal traction $\boldsymbol{p}^{\mathrm{b}}\boldsymbol{n}^{\mathrm{b}} = (\boldsymbol{n} \cdot \boldsymbol{p}^{\mathrm{b}}\boldsymbol{n}^{\mathrm{b}})\{(\boldsymbol{u}^{\mathrm{b}}/|\boldsymbol{u}^{\mathrm{b}}|)\tan\delta + \boldsymbol{n}^{\mathrm{b}}\}$. It follows that the downslope, cross-slope and normal components are

$$\left. \begin{aligned} \varepsilon p_{xx}^{\mathrm{b}}\Psi^{\mathrm{b}}\frac{\partial b}{\partial x} + \varepsilon\mu p_{xy}^{\mathrm{b}}\frac{\partial b}{\partial y} - \mu p_{xz}^{\mathrm{b}} = (\boldsymbol{n}^{\mathrm{b}} \cdot \boldsymbol{p}^{\mathrm{b}}\boldsymbol{n}^{\mathrm{b}})\left(\Delta_{\mathrm{b}}\frac{u^{\mathrm{b}}}{|\boldsymbol{u}^{\mathrm{b}}|}\tan\delta + \varepsilon\Psi\frac{\partial b}{\partial x}\right), \\ \varepsilon\mu p_{yx}^{\mathrm{b}}\Psi^{\mathrm{b}}\frac{\partial b}{\partial x} + \varepsilon p_{yy}^{\mathrm{b}}\frac{\partial b}{\partial y} - \mu p_{yz}^{\mathrm{b}} = (\boldsymbol{n}^{\mathrm{b}} \cdot \boldsymbol{p}^{\mathrm{b}}\boldsymbol{n}^{\mathrm{b}})\left(\Delta_{\mathrm{b}}\frac{v^{\mathrm{b}}}{|\boldsymbol{u}^{\mathrm{b}}|}\tan\delta + \varepsilon\frac{\partial b}{\partial y}\right), \\ \varepsilon\mu p_{zx}^{\mathrm{b}}\Psi^{\mathrm{b}}\frac{\partial b}{\partial x} + \varepsilon\mu p_{zy}^{\mathrm{b}}\frac{\partial b}{\partial y} - p_{zz}^{\mathrm{b}} = (\boldsymbol{n}^{\mathrm{b}} \cdot \boldsymbol{p}^{\mathrm{b}}\boldsymbol{n}^{\mathrm{b}})\left(\Delta_{\mathrm{b}}\frac{\varepsilon w^{\mathrm{b}}}{|\boldsymbol{u}^{\mathrm{b}}|}\tan\delta - 1\right), \end{aligned} \right\} \tag{4.12}$$

where $|\boldsymbol{u}| = (u^2 + v^2 + \varepsilon^2 w^2)^{1/2}$, the basal normal $\boldsymbol{n}^{\mathrm{b}}$ is given by

$$\Delta_{\mathrm{b}}\boldsymbol{n}^{\mathrm{b}} = \varepsilon\Psi^{\mathrm{b}}\frac{\partial b}{\partial x}\boldsymbol{g}_1^* + \varepsilon\frac{\partial b}{\partial y}\boldsymbol{g}_2^* - \boldsymbol{g}_3^*, \tag{4.13}$$

and the associated normalization factor is

$$\Delta_{\mathrm{b}} = \left\{1 + \varepsilon^2(\Psi^{\mathrm{b}})^2\left(\frac{\partial b}{\partial x}\right)^2 + \varepsilon^2\left(\frac{\partial b}{\partial y}\right)^2\right\}^{1/2}. \tag{4.14}$$

The normal pressure experienced on the basal topography, $\boldsymbol{n}^{\mathrm{b}} \cdot \boldsymbol{p}^{\mathrm{b}}\boldsymbol{n}^{\mathrm{b}}$, occurring in (4.12) takes the non-dimensional curvilinear form

$$\Delta_{\mathrm{b}}^2(\boldsymbol{n}^{\mathrm{b}} \cdot \boldsymbol{p}^{\mathrm{b}}\boldsymbol{n}^{\mathrm{b}}) = p_{zz}^{\mathrm{b}} - 2\varepsilon\mu\left(p_{xz}^{\mathrm{b}}\Psi^{\mathrm{b}}\frac{\partial b}{\partial x} + p_{yz}^{\mathrm{b}}\frac{\partial b}{\partial y}\right)$$

$$+ \varepsilon^2\left\{p_{xx}^{\mathrm{b}}(\Psi^{\mathrm{b}})^2\left(\frac{\partial b}{\partial x}\right)^2 + 2\mu p_{xy}^{\mathrm{b}}\Psi^{\mathrm{b}}\frac{\partial b}{\partial x}\frac{\partial b}{\partial y} + p_{yy}^{\mathrm{b}}\left(\frac{\partial b}{\partial y}\right)^2\right\}. \tag{4.15}$$

This completes the transformation from the coordinate independent form of §2 to curvilinear coordinates using the non-dimensional variables defined in (4.1).

5. Depth integration

The difference between the height of the free surface, $s(x, y, t)$, and the height of the basal topography, $b(x, y, t)$, defines the thickness, or depth, of the avalanche

$$h(x, y, t) = s - b, \tag{5.1}$$

measured along the normal coordinate to the reference surface. A crucial step in deriving the equations of motion for a shallow granular material is the process of integration of the mass and momentum-balance equations through the avalanche thickness. In order to perform this step it is useful to define the mean value of a function $f = f(x, y, z, t)$ (say) through the avalanche thickness

$$\overline{f} = \frac{1}{h} \int_b^s f \, \mathrm{d}z, \tag{5.2}$$

where the overbar is a shorthand notation for the depth-integrated mean value. In this paper the process of depth integrating the equations is performed before any order-of-magnitude-based estimates are made to reduce them. The reason for this is that in the original analysis of Savage & Hutter (1989), and in that of Hutter *et al.* (1993), certain terms were neglected prior to the integration process, which this study shows should not have been neglected.

The mass balance (4.3) is integrated through the avalanche depth using the Leibnitz rule to interchange the order of integration and differentiation:

$$\int_b^s \left\{ \frac{\partial}{\partial x}(u\Psi) + \frac{\partial v}{\partial y} + \frac{\partial w}{\partial z} \right\} \mathrm{d}z = \frac{\partial}{\partial x}(h\overline{u\Psi}) + \frac{\partial}{\partial y}(h\overline{v}) - \left[u\Psi\frac{\partial z}{\partial x} + v\frac{\partial z}{\partial y} - w \right]_b^s, \tag{5.3}$$

where the square bracket defines the difference of the surface and basal values of the enclosed function, $[f]_b^s = f^s - f^b$. The function contained in square brackets in (5.3) has a number of terms in common with the kinematic boundary conditions (4.9) and (4.10). Substituting for these terms and using the definition of the avalanche thickness (5.1) it follows that the depth-integrated form of the mass balance (4.3) is

$$\frac{\partial h}{\partial t} + \frac{\partial}{\partial x}(h\overline{u\Psi}) + \frac{\partial}{\partial y}(h\overline{v}) - \varepsilon\lambda\kappa'h\overline{zu\Psi^2} - \varepsilon\lambda\kappa h\overline{w\Psi} = 0. \tag{5.4}$$

The process of depth integrating the downslope component of the momentum balance (4.5) is performed in a number of stages. Integrating the first three terms of the downslope acceleration

$$a_x = \int_b^s \left\{ \frac{\partial u}{\partial t} + \frac{\partial}{\partial x}(u^2\Psi) + \frac{\partial}{\partial y}(uv) + \frac{\partial}{\partial z}(uw) \right\} \mathrm{d}z$$

$$= \frac{\partial}{\partial t}(h\overline{u}) + \frac{\partial}{\partial x}(h\overline{u^2\Psi}) + \frac{\partial}{\partial y}(h\overline{uv}) - \left[u\left(\frac{\partial z}{\partial t} + u\Psi\frac{\partial z}{\partial x} + v\frac{\partial z}{\partial y} - w \right) \right]_b^s \tag{5.5}$$

reduces to

$$a_x = \frac{\partial}{\partial t}(h\overline{u}) + \frac{\partial}{\partial x}(h\overline{u^2\Psi}) + \frac{\partial}{\partial y}(h\overline{uv}), \tag{5.6}$$

since the square-bracketed term in (5.5) is identically zero by the surface and basal kinematic conditions (4.9) and (4.10). Similarly, integrating the first three terms of

the downslope component of the pressure divergence yields

$$\int_{b}^{s}\left\{\varepsilon\frac{\partial}{\partial x}(p_{xx}\Psi)+\varepsilon\mu\frac{\partial p_{xy}}{\partial y}+\mu\frac{\partial p_{xz}}{\partial z}\right\}\mathrm{d}z$$
$$=\varepsilon\frac{\partial}{\partial x}(h\overline{p_{xx}\Psi})+\varepsilon\mu\frac{\partial}{\partial y}(h\overline{p_{xy}})-\left[\varepsilon p_{xx}\Psi\frac{\partial z}{\partial x}+\varepsilon\mu p_{xy}\frac{\partial z}{\partial y}-\mu p_{xz}\right]_{b}^{s}. \quad (5.7)$$

The function contained in square brackets is the downslope component of the negative traction vector, $\boldsymbol{pn}$. Thus, substituting for the downslope traction components from (4.11) and (4.12), the integral (5.7) reduces to

$$\int_{b}^{s}\left\{\varepsilon\frac{\partial}{\partial x}(p_{xx}\Psi)+\varepsilon\mu\frac{\partial p_{xy}}{\partial y}+\mu\frac{\partial p_{xz}}{\partial z}\right\}\mathrm{d}z$$
$$=\varepsilon\frac{\partial}{\partial x}(h\overline{p_{xx}\Psi})+\varepsilon\mu\frac{\partial}{\partial y}(h\overline{p_{xy}})+\left(\Delta_{b}(u^{b}/|\boldsymbol{u}^{b}|)\tan\delta+\varepsilon\Psi\frac{\partial b}{\partial x}\right)(\boldsymbol{n}^{b}\cdot\boldsymbol{p}^{b}\boldsymbol{n}^{b}), \quad (5.8)$$

where the Coulomb dry-friction law and the downslope component of the normal basal pressure enter through the boundary conditions. Note, that the error in the analysis of Savage & Hutter (1989) and Hutter *et al.* (1993) occurred at this point, as it was wrongly assumed that to first order in ε the downslope component of the normal basal pressure did not enter through the basal boundary conditions.

The cross-slope and normal components of the acceleration and pressure gradients are depth integrated in exactly the same way as the downslope components. It follows that the depth-integrated downslope, cross-slope and normal components of the momentum balances (4.5)–(4.7) are

$$\frac{\partial}{\partial t}(h\overline{u})+\frac{\partial}{\partial x}(h\overline{u^2\Psi})+\frac{\partial}{\partial y}(h\overline{uv})-\varepsilon\lambda\kappa'h\overline{zu^2\Psi^2}-2\varepsilon\lambda\kappa h\overline{uw\Psi}$$
$$=h\sin\zeta-\left(\Delta_{b}\frac{u^{b}}{|\boldsymbol{u}^{b}|}\tan\delta+\varepsilon\Psi^{b}\frac{\partial b}{\partial x}\right)(\boldsymbol{n}^{b}\cdot\boldsymbol{p}^{b}\boldsymbol{n}^{b})$$
$$-\varepsilon\frac{\partial}{\partial x}(h\overline{p_{xx}\Psi})-\varepsilon\mu\frac{\partial}{\partial y}(h\overline{p_{xy}})+\varepsilon^2\lambda\kappa'h\overline{z\,p_{xx}\Psi^2}+2\varepsilon\mu\lambda\kappa h\overline{p_{xz}\Psi}, \quad (5.9)$$

$$\frac{\partial}{\partial t}(h\overline{v})+\frac{\partial}{\partial x}(h\overline{uv\Psi})+\frac{\partial}{\partial y}(h\overline{v^2})-\varepsilon\lambda\kappa'h\overline{z\,uv\Psi^2}-\varepsilon\lambda\kappa h\overline{vw\Psi}$$
$$=-\left(\Delta_{b}\frac{v^{b}}{|\boldsymbol{u}^{b}|}\tan\delta+\varepsilon\frac{\partial b}{\partial y}\right)(\boldsymbol{n}^{b}\cdot\boldsymbol{p}^{b}\boldsymbol{n}^{b})$$
$$-\varepsilon\mu\frac{\partial}{\partial x}(h\overline{p_{xy}\Psi})-\varepsilon\frac{\partial}{\partial y}(h\overline{p_{yy}})+\varepsilon^2\lambda\mu\kappa'h\overline{z\,p_{xy}\Psi^2}+\varepsilon\lambda\mu\kappa h\overline{p_{yz}\Psi}, \quad (5.10)$$

$$\varepsilon\left\{\frac{\partial}{\partial t}(h\overline{w})+\frac{\partial}{\partial x}(h\overline{uw\Psi})+\frac{\partial}{\partial y}(h\overline{vw})\right\}-\varepsilon^2\lambda\kappa'h\overline{z\,uw\Psi^2}-\lambda\kappa h\overline{(\varepsilon^2w^2-u^2)\Psi}$$
$$=-h\cos\zeta-\left(\Delta_{b}\frac{\varepsilon w^{b}}{|\boldsymbol{u}^{b}|}\tan\delta-1\right)(\boldsymbol{n}^{b}\cdot\boldsymbol{p}^{b}\boldsymbol{n}^{b})$$
$$-\varepsilon\mu\frac{\partial}{\partial x}(h\overline{p_{xz}\Psi})-\varepsilon\mu\frac{\partial}{\partial y}(h\overline{p_{yz}})+\varepsilon^2\lambda\kappa'h\overline{z\,p_{xz}\Psi^2}+\varepsilon\lambda\kappa h\overline{(p_{zz}-p_{zz})\Psi}, \quad (5.11)$$

respectively. The formal depth-integration process is now complete. The depth-integrated mass balance (5.4), and the depth integrated downslope and cross-slope

momentum balances, (5.9) and (5.10), form the basis of the shallow granular flow equations.

6. Ordering

Landslides, rock falls and snow avalanches all have the common geometrical property that typical down- and cross-slope lengths are much larger than the typical normal thicknesses. The shallowness of these natural flows is now exploited to reduce the governing equations, of §§ 4 and 5, in a consistent and rational manner. The so-called *shallowness assumption* assumes that the aspect ratio of the avalanche is small:

$$\varepsilon = \frac{H}{L} \ll 1. \tag{6.1}$$

This assumption alone is not sufficient to derive a reduced theory as the resulting leading-order equations in ε neglect the constitutive properties of the granular material and are consequently far too simple. Following Greve *et al.* (1994), the non-dimensional parameters λ and μ, defined in equations (4.2), are assumed to be of magnitude

$$\lambda = O(\varepsilon^{\alpha}), \quad \mu = O(\varepsilon^{\beta}), \tag{6.2}$$

where $0 < \alpha < 1$ and $0 < \beta < 1$ are realistic for typical reference surface curvatures and coefficients of basal friction. It follows from (4.4) and (4.14) that the functions

$$\Psi = 1 + O(\varepsilon^{1+\alpha}), \quad \Delta_{\mathrm{b}} = 1 + O(\varepsilon^{2}). \tag{6.3}$$

Applying the above ordering of the non-dimensional parameters it follows that the depth-integrated mass-balance equation (5.3) reduces to

$$\frac{\partial h}{\partial t} + \frac{\partial}{\partial x}(h\bar{u}) + \frac{\partial}{\partial y}(h\bar{v}) = 0 + O(\varepsilon^{1+\alpha}), \tag{6.4}$$

which, as Greve *et al.* (1994) pointed out, takes exactly the same form as if it were in Cartesian coordinates.

To obtain a realistic theory, which includes some constitutive properties of the granular material, the downslope and cross-slope components of the depth-integrated momentum balance, (5.9) and (5.10), must be approximated to leading and first order in the small parameter ε. These equations contain a term that is multiplied by the factor $\boldsymbol{n}^{\mathrm{b}} \cdot \boldsymbol{p}^{\mathrm{b}} \boldsymbol{n}^{\mathrm{b}}$, which from the normal component of the momentum balance (5.11) is

$$\boldsymbol{n}^{\mathrm{b}} \cdot \boldsymbol{p}^{\mathrm{b}} \boldsymbol{n}^{\mathrm{b}} = h \cos\zeta + \lambda\kappa h\overline{u^2} + O(\varepsilon), \tag{6.5}$$

to order ε, or

$$\boldsymbol{n}^{\mathrm{b}} \cdot \boldsymbol{p}^{\mathrm{b}} \boldsymbol{n}^{\mathrm{b}} = h \cos\zeta + O(\varepsilon^{\alpha}), \tag{6.6}$$

to order ε^{α}. Recalling that $\tan\delta = O(\varepsilon^{\beta})$ (by definition) it follows from (6.5) and (6.6) that the depth-integrated momentum balances in the downslope (5.9) and cross-

slope (5.10) directions reduce to

$$\frac{\partial}{\partial t}(h\overline{u}) + \frac{\partial}{\partial x}(h\overline{u^2}) + \frac{\partial}{\partial y}(h\overline{uv})$$

$$= h\sin\zeta - \frac{u^{\mathrm{b}}}{|\boldsymbol{v}^{\mathrm{b}}|}h\tan\delta(\cos\zeta + \lambda\kappa\overline{u^2}) - \varepsilon\frac{\partial}{\partial x}(h\overline{p_{xx}}) - \varepsilon\cos\zeta h\frac{\partial b}{\partial x} + O(\varepsilon^{1+\gamma}), \tag{6.7}$$

$$\frac{\partial}{\partial t}(h\overline{v}) + \frac{\partial}{\partial x}(h\overline{uv}) + \frac{\partial}{\partial y}(h\overline{v^2})$$

$$= -\frac{v^{\mathrm{b}}}{|\boldsymbol{v}^{\mathrm{b}}|}h\tan\delta(\cos\zeta + \lambda\kappa\overline{u^2}) - \varepsilon\frac{\partial}{\partial y}(h\overline{p_{yy}}) - \varepsilon\cos\zeta h\frac{\partial b}{\partial y} + O(\varepsilon^{1+\gamma}), \tag{6.8}$$

where $\boldsymbol{v} = (u, v, 0)^{\mathrm{T}}$ is the two-dimensional tangential velocity and $\gamma = \min(\alpha, \beta)$ satisfies the inequality $0 < \gamma < 1$. The term $(\boldsymbol{v}^{\mathrm{b}}/|\boldsymbol{v}^{\mathrm{b}}|)h\tan\delta\lambda\kappa\overline{u^2} = O(\varepsilon^{\alpha+\beta})$ is assumed to contribute to the leading- and first-order balances. That is, it is assumed that $\alpha+\beta \leqslant 1$. If, however, $1 < \alpha+\beta < 1+\gamma$, or, $\alpha+\beta \geqslant 1+\gamma$, then this term can be neglected and the depth-integrated downslope and cross-slope momentum balances are accurate to order $\varepsilon^{\alpha+\beta}$, or $\varepsilon^{1+\gamma}$, respectively. Further reduction of (6.7) and (6.8) requires constitutive information about the pressure tensor $\boldsymbol{p}$ and the depth-integrated tangential velocity $\overline{\boldsymbol{v}}$.

The normal component of momentum balance (4.7) reduces to

$$\frac{\partial p_{zz}}{\partial z} = -\cos\zeta + O(\varepsilon^{\alpha}). \tag{6.9}$$

Integrating with respect to z and applying the free surface boundary condition (4.11), that $p_{zz}^{\mathrm{s}} = 0 + O(\varepsilon^{1+\beta})$, it follows that

$$p_{zz} = (s - z)\cos\zeta + O(\varepsilon^{\alpha}), \tag{6.10}$$

and $p_{zz}^{\mathrm{b}} = h\cos\zeta + O(\varepsilon^{\alpha})$, consistent with (6.6) and (4.12). Note that the pressure p_{zz} need only be approximated to order ε^{α} as it is used to simplify the depth-integrated downslope and cross-slope pressure terms, $\overline{p_{xx}}$ and $\overline{p_{yy}}$, which are already order ε terms in (6.7) and (6.8).

7. Mohr–Coulomb closure

The Savage–Hutter theory assumes that a very simple state of stress prevails within the avalanche. Given principal stresses p_1, p_2, p_3, one of these, (p_1 say), is assumed to lie in the cross-slope direction, $p_1 = p_{yy}$, which is consistent with the notion that the dominant deformation takes place in the downslope direction. In addition it is assumed that one of the other two principal stresses (which now lie in the xz-plane) is equal in magnitude to p_1, i.e. $p_1 = p_2$ or p_3. This assumption reduces the three-dimensional Mohr circle of stress to a single two-dimensional Mohr circle of stress. The principal stresses, p_x and p_z, in the xz-plane are given by

$$p_x, p_z = \tfrac{1}{2}(p_{xx} + p_{zz}) \pm \tfrac{1}{2}\sqrt{(p_{xx} - p_{zz})^2 + 4\mu^2 p_{xz}^2}, \tag{7.1}$$

and the cross-slope principal stress $p_{yy} = p_x$ or p_z depending on the nature of the deformation.

In the original Savage & Hutter (1991) theory the basal normal pressure equals p_{zz}^b and the shear stress equals $-p_{xz}^b$. Two Mohr stress circles can be constructed that satisfy both the basal sliding law and the internal yield criterion simultaneously. The basal downslope pressure p_{xx}^b can therefore assume two values, one on the larger circle, $p_{xx}^b > p_{zz}^b$, and one on the smaller circle, $p_{xx}^b \leqslant p_{zz}^b$, which are associated with *passive* and *active* stress states, respectively. There are four possible values for the principal stresses, p_x^b and p_z^b, and hence four values for the basal cross-slope pressure p_{yy}^b.

The earth pressure coefficients K_x^b and K_y^b are defined as the ratio of the basal downslope and cross-slope pressures to the normal basal pressure:

$$K_x^b = p_{xx}^b/p_{zz}^b, \quad K_y^b = p_{yy}^b/p_{zz}^b. \tag{7.2}$$

Savage & Hutter (1989) used elementary geometrical arguments to determine the value of K_x^b, and Hutter *et al.* (1993) used the Mohr circle representations (7.1) to construct K_y^b as a function of the internal and basal angles of friction:

$$K_{x_{\mathrm{act/pas}}}^b = 2\sec^2\phi(1 \mp \{1 - \cos^2\phi\sec^2\delta\}^{1/2}) - 1, \tag{7.3}$$

$$(K_{y_{\mathrm{act/pas}}}^x)^b = \tfrac{1}{2}(K_x^b + 1 \mp \{(K_x^b - 1)^2 + 4\tan^2\delta\}^{1/2}), \tag{7.4}$$

which are real if and only if $\delta \leqslant \phi$. Furthermore, it is relatively easy to demonstrate from (7.3) and (7.4) that they are ordered in the following way: $K_{x_{\mathrm{act}}} \leqslant K_{x_{\mathrm{pas}}}$ and $K_{y_{\mathrm{act}}}^{x_{\mathrm{act}}} \leqslant K_{y_{\mathrm{act}}}^{x_{\mathrm{pas}}} \leqslant K_{y_{\mathrm{pas}}}^{x_{\mathrm{act}}} \leqslant K_{y_{\mathrm{pas}}}^{x_{\mathrm{pas}}}$. Note that to order ε^β the cross-slope earth pressure coefficients can be reduced to $K_y = K_x$, or 1, but this form is not adopted as it destroys the natural ordering.

There is no explicit flow rule or other criterion within the model to uniquely determine which value of the earth pressure coefficient is associated with a particular deformation. Savage & Hutter (1989) made the ad hoc definition that the downslope earth pressure K_x was *active* during a downslope dilatational motion and *passive* during a downslope compressional motion:

$$K_x^b = \begin{cases} K_{x_{\mathrm{act}}}, & \partial u/\partial x > 0, \\ K_{x_{\mathrm{pas}}}, & \partial u/\partial x < 0. \end{cases} \tag{7.5}$$

Similarly, in the cross-slope direction the four stress ratios were distinguished from one another (Hutter *et al.* 1993) by considering whether the downslope and the cross-slope deformation were dilatational or compressional:

$$K_y^b = \begin{cases} K_{y_{\mathrm{act}}}^{x_{\mathrm{act}}}, & \partial u/\partial x > 0, & \partial v/\partial y > 0, \\ K_{y_{\mathrm{act}}}^{x_{\mathrm{pas}}}, & \partial u/\partial x < 0, & \partial v/\partial y > 0, \\ K_{y_{\mathrm{pas}}}^{x_{\mathrm{act}}}, & \partial u/\partial x > 0, & \partial v/\partial y < 0, \\ K_{y_{\mathrm{pas}}}^{x_{\mathrm{pas}}}, & \partial u/\partial x < 0, & \partial v/\partial y < 0. \end{cases} \tag{7.6}$$

In three dimensions the basal shear stress is no longer parallel to the downslope direction, since $\mu p_{xz}^b = (u^b/|\boldsymbol{v}^b|)p_{zz}^b\tan\delta + O(\varepsilon)$ and $\mu p_{yz}^b = (v^b/|\boldsymbol{v}^b|)p_{zz}^b\tan\delta + O(\varepsilon)$ in (4.12) are both dependent on the direction of the basal velocity. It follows that the arguments used to derive the earth pressure coefficients fail unless $u^b \gg v^b$, as pointed out in Hutter *et al.* (1993). However, Koch *et al.* (1994) still get good agreement between theory and experiment even on slopes without lateral confinement. In this paper it is therefore assumed that

$$p_{xx}^b = K_x^b p_{zz}^b, \quad p_{yy}^b = K_y^b p_{zz}^b, \tag{7.7}$$

where K_x^{b} and K_y^{b} are given by (7.3), (7.4). At the traction free surface of the avalanche the Mohr–Coulomb yield criterion collapses to a single point to order ε^{α} and the downslope and cross-slope normal surface pressures are

$$p_{xx}^{\mathrm{s}} = 0 + O(\varepsilon^{\gamma}), \quad p_{yy}^{\mathrm{s}} = 0 + O(\varepsilon^{\gamma}). \tag{7.8}$$

The Savage–Hutter theory assumes that the downslope and cross-slope pressures vary linearly with the normal pressure through the depth of the avalanche. This is fulfilled to leading order provided

$$p_{xx} = K_x p_{zz} + O(\varepsilon^{\gamma}), \quad p_{yy} = K_y p_{zz} + O(\varepsilon^{\gamma}), \tag{7.9}$$

where the earth pressure coefficients K_x and K_y are equal to K_x^{b} and K_y^{b}. Substituting for the normal pressure p_{zz} from (6.10) and integrating through the depth of the avalanche it follows that the depth-integrated pressures are $h\overline{p_{xx}} = K_x \cos\zeta h^2/2 + O(\varepsilon^{\gamma})$ and $h\overline{p_{yy}} = K_y \cos\zeta h^2/2 + O(\varepsilon^{\gamma})$. Substituting these expressions into the depth-integrated downslope (6.7) and cross-slope (6.8) momentum balances yields

$$\frac{\partial}{\partial t}(h\overline{u}) + \frac{\partial}{\partial x}(h\overline{u^2}) + \frac{\partial}{\partial y}(h\overline{uv}) = h\sin\zeta - \frac{u^{\mathrm{b}}}{|\boldsymbol{v}^{\mathrm{b}}|}h\tan\delta(\cos\zeta + \lambda\kappa\overline{u^2})$$
$$- \varepsilon\frac{\partial}{\partial x}(\cos\zeta K_x h^2/2) - \varepsilon\cos\zeta h\frac{\partial b}{\partial x} + O(\varepsilon^{1+\gamma}), \tag{7.10}$$

$$\frac{\partial}{\partial t}(h\overline{v}) + \frac{\partial}{\partial x}(h\overline{uv}) + \frac{\partial}{\partial y}(h\overline{v^2}) = -\frac{v^{\mathrm{b}}}{|\boldsymbol{v}^{\mathrm{b}}|}h\tan\delta(\cos\zeta + \lambda\kappa\overline{u^2})$$
$$- \varepsilon\frac{\partial}{\partial y}(\cos\zeta K_y h^2/2) - \varepsilon\cos\zeta h\frac{\partial b}{\partial y} + O(\varepsilon^{1+\gamma}). \tag{7.11}$$

Note that the terms involving the earth pressure coefficients can be simplified further since $\zeta = \zeta(x)$ and $\partial\zeta/\partial x = -\lambda\kappa$. In addition, provided the earth pressure coefficients satisfy the relations $\partial K_x/\partial x = O(\varepsilon^{\gamma})$ and $\partial K_y/\partial y = O(\varepsilon^{\gamma})$, then

$$\frac{\partial}{\partial x}(\tfrac{1}{2}K_x h^2 \cos\zeta) = hK_x \cos\zeta\frac{\partial h}{\partial x} + O(\varepsilon^{\gamma}),$$
$$\frac{\partial}{\partial y}(\tfrac{1}{2}K_y h^2 \cos\zeta) = hK_y \cos\zeta\frac{\partial h}{\partial y} + O(\varepsilon^{\gamma}).$$

The constitutive properties that are used in the Savage–Hutter theory provide no link between the stress and the strain-rate and therefore no means of computing the velocity profile through the depth of the avalanche. Instead the Boussinesq assumption is made:

$$\overline{u} = u^{\mathrm{b}} + O(\varepsilon^{1+\gamma}), \quad \overline{v} = v^{\mathrm{b}} + O(\varepsilon^{1+\gamma}), \tag{7.12}$$

which is supported by recent measurements in large-scale dry snow (Dent *et al.* 1998) and ping-pong ball avalanches (Keller *et al.* 1998). This implies that the tangential velocity components are independent of depth to leading and first order in ε, and allows the averages to be factorized:

$$\overline{u^2} = (u^{\mathrm{b}})^2 + O(\varepsilon^{1+\gamma}), \quad \overline{uv} = u^{\mathrm{b}}v^{\mathrm{b}} + O(\varepsilon^{1+\gamma}), \quad \overline{v^2} = (v^{\mathrm{b}})^2 + O(\varepsilon^{1+\gamma}). \tag{7.13}$$

It follows from (7.12) that the continuity equation (6.4) reduces to

$$\frac{\partial h}{\partial t} + \frac{\partial}{\partial x}(hu) + \frac{\partial}{\partial y}(hv) = 0, \qquad (7.14)$$

to order $\varepsilon^{1+\gamma}$, where the superscript 'b' is now dropped. The continuity equation (7.14) can be used to simplify the acceleration terms in the downslope and cross-slope momentum balances, (7.10) and (7.11), yielding, to order $\varepsilon^{1+\gamma}$,

$$h\frac{\mathrm{d}u}{\mathrm{d}t} = h\sin\zeta - \frac{u}{|\boldsymbol{u}|}h\tan\delta(\cos\zeta + \lambda\kappa u^2) - \varepsilon h\cos\zeta\left(K_x\frac{\partial h}{\partial x} + \frac{\partial b}{\partial x}\right), \qquad (7.15)$$

$$h\frac{\mathrm{d}v}{\mathrm{d}t} = -\frac{v}{|\boldsymbol{u}|}h\tan\delta(\cos\zeta + \lambda\kappa u^2) - \varepsilon h\cos\zeta\left(K_y\frac{\partial h}{\partial y} + \frac{\partial b}{\partial y}\right), \qquad (7.16)$$

where $\mathrm{d}/\mathrm{d}t = \partial/\partial t + u\partial/\partial x + v\partial/\partial y$. The depth-integrated momentum balances, (7.15) and (7.16), are satisfied when either the avalanche thickness is equal to zero,

$$h = 0, \qquad (7.17)$$

or when

$$\frac{\mathrm{d}u}{\mathrm{d}t} = \sin\zeta - \frac{u}{|\boldsymbol{u}|}\tan\delta(\cos\zeta + \lambda\kappa u^2) - \varepsilon\cos\zeta\left(K_x\frac{\partial h}{\partial x} + \frac{\partial b}{\partial x}\right), \qquad (7.18)$$

$$\frac{\mathrm{d}v}{\mathrm{d}t} = -\frac{v}{|\boldsymbol{u}|}\tan\delta(\cos\zeta + \lambda\kappa u^2) - \varepsilon\cos\zeta\left(K_y\frac{\partial h}{\partial y} + \frac{\partial b}{\partial y}\right). \qquad (7.19)$$

Given material parameters δ, ϕ, a reference surface $\zeta(x)$ and basal topography $b(x,y)$ (in regions where the thickness $h \neq 0$), the system of equations (7.14), (7.18) and (7.19) allow the three independent variables h, u and v to be computed, once initial conditions and boundary conditions at the edge of the avalanche domain are prescribed. Of particular interest to avalanche modelling is the case when the initial thickness of an avalanche body Ω is zero along the boundary $\partial\Omega$. The momentum balances, (7.15) and (7.16), are trivially satisfied on the boundary (7.17), and the equation for the thickness (7.14) reduces to $\mathrm{d}h/\mathrm{d}t = 0$. It follows that if the thickness on $\partial\Omega$ is initially zero then it remains zero throughout the motion and advects with the same velocity as the adjacent avalanche by continuity. The degenerate boundary condition $h = 0$ on $\partial\Omega$ is equivalent to the physical boundary condition that the edge of the avalanche is traction free, which is appropriate.

An equivalent system of equations to the original one-dimensional Savage & Hutter (1989) equations can be recovered by setting all gradients $\partial/\partial y = 0$, the cross-slope velocity $v = 0$ and the inclination angle ζ constant (which implies $\kappa = 0$) in (7.14), (7.18) and (7.19). The resulting equations are identical to those of Savage & Hutter (1989) except for the basal topography gradient term, which equals $-\varepsilon\cos\zeta\partial b/\partial x$ here and $-\varepsilon\cos\zeta K_x\partial b/\partial x$ in Savage & Hutter (1989). The extra factor K_x stems from an error made by Savage & Hutter (1989) in the depth-integration and ordering process, which was mentioned in §5. The same error was made by Hutter *et al.* (1993) in two-dimensions. A reduction to the system of equations derived for quasi-two-dimensional basal topography (Greve *et al.* 1994) is achieved by setting $b = 0$.

8. Comparison with laboratory experiments

A laboratory experiment on a chute with complex basal topography has been performed to test the validity of the theoretical model. A simple reference surface is
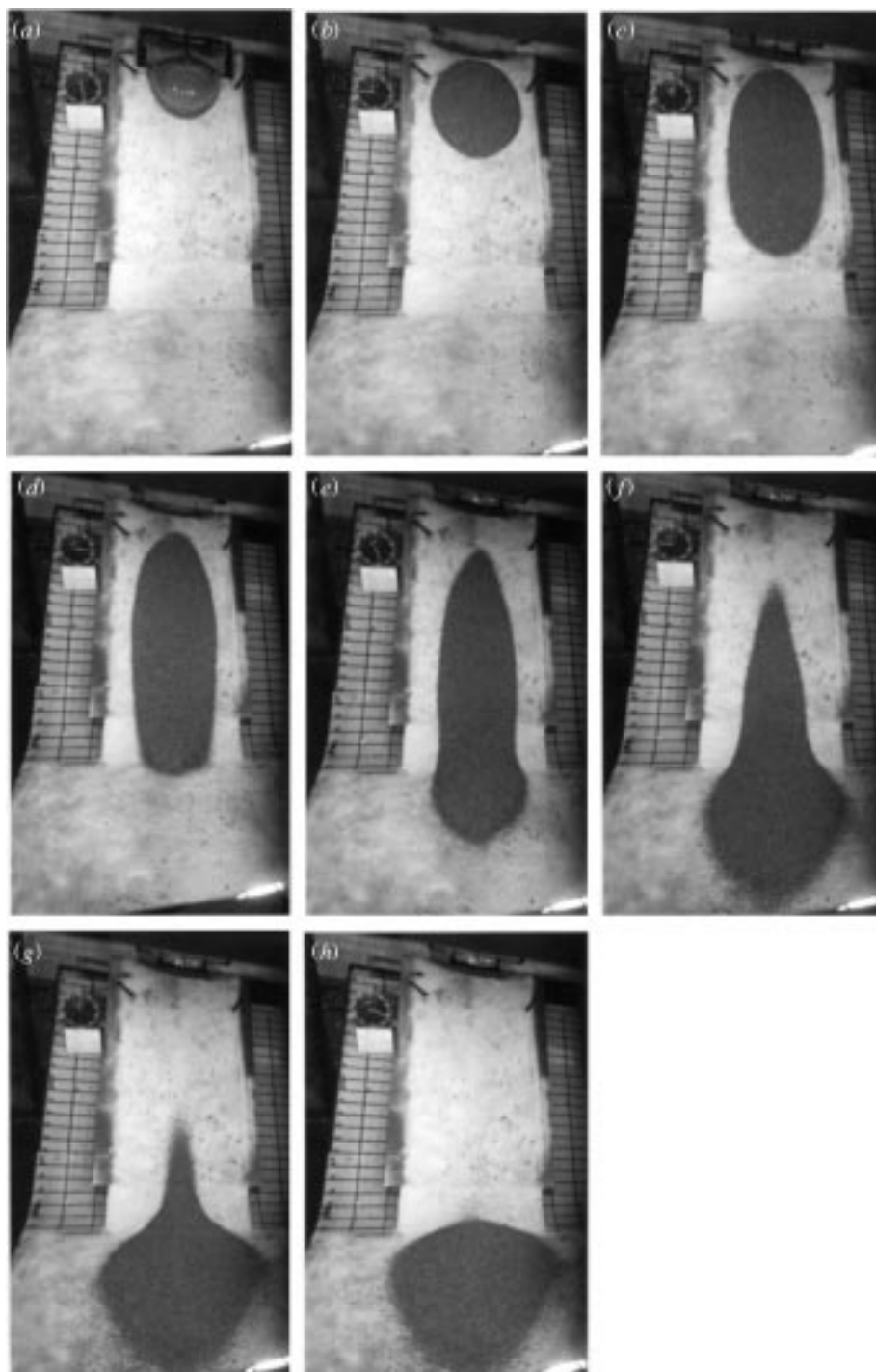
Figure 3. An experimental image sequence from experiment V02 showing the deformation of the avalanche at approximately equally spaced time intervals of 0.25 s. The large hand of the clock performs one revolution per second. The sequence begins at (*a*) and ends at (*h*).
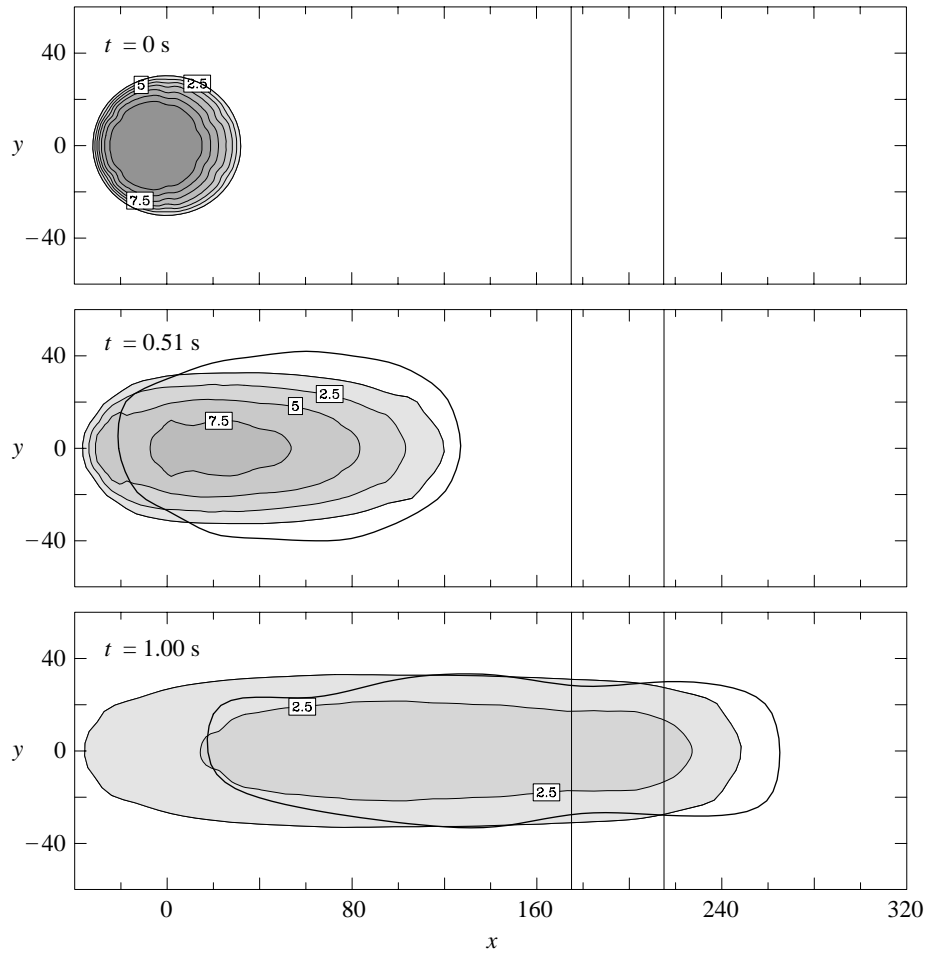
Figure 4. The computed avalanche thickness is illustrated at five time intervals using 'unrolled' projected curvilinear coordinates (x, y). Contours of equal thickness are indicated in centimetres and thickness ranges are differently shaded. The time is indicated in the top left-hand corner and all lengths are in centimetres. The solid lines at $x = 175$ and $x = 215$ cm indicate the position of the transition zone. The $40°$ inclined parabolic section lies on the left and the horizontal plane on the right of each panel. The line $y = 0$ is the Talweg. The thick solid line indicates the position of the avalanche edge in the laboratory experiment (V02).

defined, which consists of an inclined plane $(\zeta = 40°)$ that is connected to a horizontal run-out zone $(\zeta = 0°)$ by a cylindrical transition zone. The x-axis is aligned with the direction of steepest descent of the reference surface and the y-axis points in the cross-slope direction. Superposed on the inclined section of the chute is a shallow parabolic cross-slope topography, $b = y^2/(2R)$ with $R = 110$ cm, which forms a channel that partly confines the avalanche motion. The inclined parabolic chute lies in the range $x < 175$ cm, the plane run-out zone lies in the range $x > 215$ cm and a transition zone smoothly joins the two regions. The channel is symmetric about the line $y = 0$, and this line also represents the Talweg, the set of points with the minimum height above the curvilinear surface $z = 0$. The parabolic channel and run-out
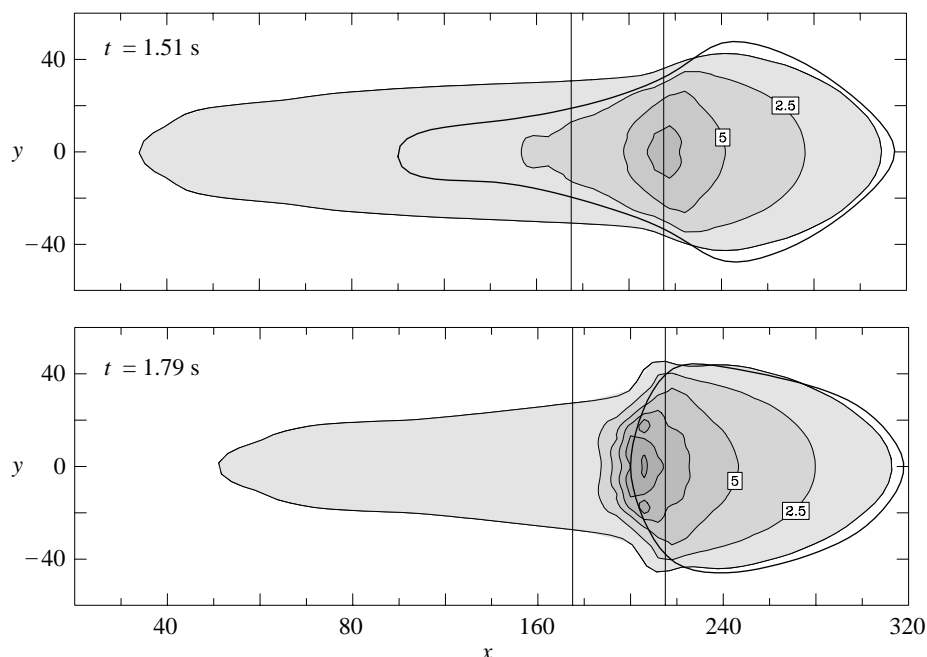
Figure 4. (*Cont.*)

plane are constructed from sheet steel and the smooth transition is made from wood and modelling plaster. The whole chute is painted to give it an even finish.

The experiment (V02) is performed with quartz chips of mean diameter 2–4 mm, (Quartz0) internal angle of friction $\phi = 40°$ and basal angle of friction $\delta = 30°$. The granular material is released from rest on the parabolic inclined section of the chute by means of a perspex cap that opens rapidly at $t = 0$ seconds. The cap has a spherical free surface, which is fitted to the basal chute topography. The projection of this line of intersection onto the reference surface is approximately elliptical in shape. The major axis of the ellipse is of length 32 cm and the maximum height of the cap above the reference surface is 22 cm.

The avalanche flow is photographed with a high-speed Canon F1 camera that takes 5, 10 or 15 frames per second. A sequence of pictures taken at approximately $\frac{1}{4}$ s intervals is shown in figure 3. The clock is shown in the top-left-hand corner of each image and the large hand performs one revolution per second. Figure 3 clearly shows that once the cap is opened, the avalanche accelerates and spreads rapidly in the downslope direction, while it is channelled by the parabolic cross-slope profile. As the avalanche enters the run out zone it decelerates rapidly and is able to spread out laterally once the partial confinement of the topography ceases. This leads to a characteristic *tadpole* shape, after approximately 1.25 s, in which the tail of the avalanche is reducing in width due to the channelling effect of the parabolic cross-slope topography and the head of the avalanche is expanding in width on the run-out plane. The avalanche comes to rest after 1.79 s. Photogrammetric techniques have been used to determine the position of the avalanche boundary at a number of time intervals during the avalanche motion in order to provide a comparison with computed solutions.

The two-dimensional Lagrangian numerical method (Koch *et al.* 1994) has been improved and extended to solve the system of equations derived in this paper. Figure 4 shows a sequence of avalanche thickness contours computed with this algorithm at times $t = 0$, 0.51, 1.0, 1.51 and 1.79 s. The results are plotted in projected curvilinear coordinates (x, y) and all units are in centimetres. The vertical lines at $x = 175$ cm and $x = 215$ cm indicate the beginning and end of the transition zone, respectively. The inclined plane is on the left of each panel and the horizontal run-out zone is on the right. The top panel shows the initial configuration of the avalanche and in the subsequent panels an additional thick solid line indicates the position of the experimental avalanche boundary, which provides a direct comparison with the computed boundary at the edge of the shaded domains.

Once the cap is released the avalanche spreads rapidly in the downslope direction ($t = 0.51$ s) and the computed solution lies slightly behind the laboratory experiment. The lateral basal topography gradient is almost in exact balance with the cross-slope earth pressure gradient and the lateral velocity is consequently very small. As the avalanche continues to spread in the downslope direction ($t = 1$ s) the thickness gradients are reduced and the lateral topography gradients begin to channel the avalanche. The avalanche has developed the characteristic tadpole-like form at $t = 1.51$ s. However, the avalanche tail has moved only 20 cm from its initial position and the tadpole's tail is therefore considerably more elongated than in the experiment. At $t = 1.79$ s, when the laboratory avalanche comes to rest, the slowness of the computed avalanche tail becomes even more apparent.

There are a number of factors which contribute to the apparent slow tail motion. Firstly at the avalanche boundary the thickness is of the order of one grain size, i.e. 2–4 mm, and not zero as assumed in the computed solution. The finite grain size can have a significant effect on the apparent position of the boundary in regions where the avalanche is thin and the thickness gradients are small, for instance in the avalanche tail. In the fourth panel of figure 4 the 2.5 cm thickness contour intersects the centre-line at approximately $x = 150$ cm and the 0 cm contour lies at -10 cm. A linear interpolation between these two points suggests that the avalanche is of the order of one grain size thick at $x = 2.8$–15 cm, which provides an ad hoc correction to the boundary position. This accounts for 11–22% of the discrepancy between the computed position and actual position of the avalanche boundary at $x = 110$ cm.

The most likely cause for the slow tail motion is that the basal sliding law is considerably more complicated than simple Coulomb dry friction (2.7) with constant bed-friction angle. There are good reasons to suppose that rate-dependent effects may be important. With the Coulomb sliding model, the centre of mass of the avalanche accelerates at a constant rate on an infinitely long inclined plane and its velocity increases linearly without bound. Physically, one would expect that rate-dependent friction becomes important and brings the avalanche to a finite *terminal* velocity. This can be achieved by including velocity dependent Voellmy drags of the form $-\rho_0 c_2 |\boldsymbol{v}| \boldsymbol{v}$ to resist the motion. During the spreading phase (around $t = 1$ s) the avalanche front has velocities approaching 10 m s^{-1}, while the tail is almost stationary. These velocity magnitudes are large enough for the Voellmy drags $\rho_0 c_2 |\boldsymbol{v}|^2 \sim 10^2 \text{ kg m}^{-1} \text{ s}^{-2}$ to become important relative to the Coulomb friction $\rho_0 gh \tan \delta \cos \zeta \sim 10^3 \text{ kg m}^{-1} \text{ s}^{-2}$ at the front of the avalanche. Air drag $\rho_a c_a |\boldsymbol{v}|^2 \sim 10^{-1} \text{ kg m}^{-1} \text{ s}^{-2}$, however, is not important at these laboratory speeds, but may play a role in geophysical flows where much higher speeds are attained. Lab-

oratory measurements also suggest there is a range of bed-friction angles, associated with the transition from static to dynamic friction, that can produce a reduction of 5° during steady dynamic deformations (Hungr & Morgenstern 1984*a*, *b*). This may also be important. Furthermore, at rough boundaries collisional interactions may produce large *granular temperatures* that fluidize the flow and reduce the friction. It is clear that there are a number of competing effects and that the tribology of such rapidly moving and evolving surfaces is not well understood. Further experiments must be performed before a universally valid drag law can be determined, but it is interesting to note that deviations from the Coulomb sliding law with constant bed-friction angle introduces a scale dependence into the theory. That is, the solution of similar problems with different length-scales will produce different results.

In order to demonstrate that a change in the bed-friction sliding law can at least qualitatively bring the theory and experiment into agreement, the numerical computations have been repeated using a variable bed-friction angle. In the front quarter of the avalanche the bed-friction angle is constant as before, but reduces linearly in the rear three quarters:

$$\delta = \begin{cases} \delta_0, & x \geqslant x_{\mathrm{f}} - \frac{1}{4}(x_{\mathrm{f}} - x_{\mathrm{r}}), \\ \delta_0 - m_\delta((x_{\mathrm{f}} - x) - \frac{1}{4}(x_{\mathrm{f}} - x_{\mathrm{r}})), & x < x_{\mathrm{f}} - \frac{1}{4}(x_{\mathrm{f}} - x_{\mathrm{r}}), \end{cases} \tag{8.1}$$

where $\delta_0 = 30°$ is the constant bed-friction angle, $m_\delta = 10° \ \mathrm{m}^{-1}$ is the bed-friction reduction factor and x_{f} and x_{r} are the positions of the front and rear of the avalanche, respectively.

The avalanche thickness distributions computed using the modified bed-friction relation (8.1) are illustrated in figure 5. After 0.51 s the solution is almost identical to the constant bed-friction angle simulation in figure 4. It is only after 1 s that significant differences start to appear. The reduced bed-friction angle in the avalanche tail allows the rear of the avalanche to accelerate more rapidly under the action of gravity and the agreement with the experimental boundary is correspondingly far better. The tadpole shape is reproduced very well and the avalanche comes to rest at approximately 1.79 s in almost exact agreement with the experimentally determined avalanche boundary. This demonstrates that a modification to the basal frictional forces is sufficient to explain the slow tail motion, although it is emphasized that further basic research on the physics of friction in avalanches is necessary before a universally applicable law can be determined.

The state of stress in the down and cross-slope directions is illustrated in figures 6 and 7 at the same times as the avalanche thickness. In each panel the deformed Lagrangian numerical grid is drawn and the individual grid cells are shaded to show which value of the earth pressure coefficient is activated at any given time. Recalling the relations (7.5) and (7.6), these states are synonymous with the local deformation of the grid cell. The highest velocities are attained at the front of the avalanche and this predominantly divergent motion gives rise to active downslope earth pressures at $t = 0.51$ s. Initially, the avalanche expands laterally, but as the thickness gradients are eroded the effect of the basal topography $\partial b/\partial y$ takes over and the avalanche begins to be compressed laterally. The transition from cross-slope expansion to compression, with some grid cells active and some passive, is shown in figure 7 at $t = 0.51$ s.

After 1 s has elapsed the avalanche spans all three sections of the chute and all the earth pressure states in the downslope and cross-slope directions are activated. The front, or *nose*, of the avalanche lies on the horizontal plane and diverges in
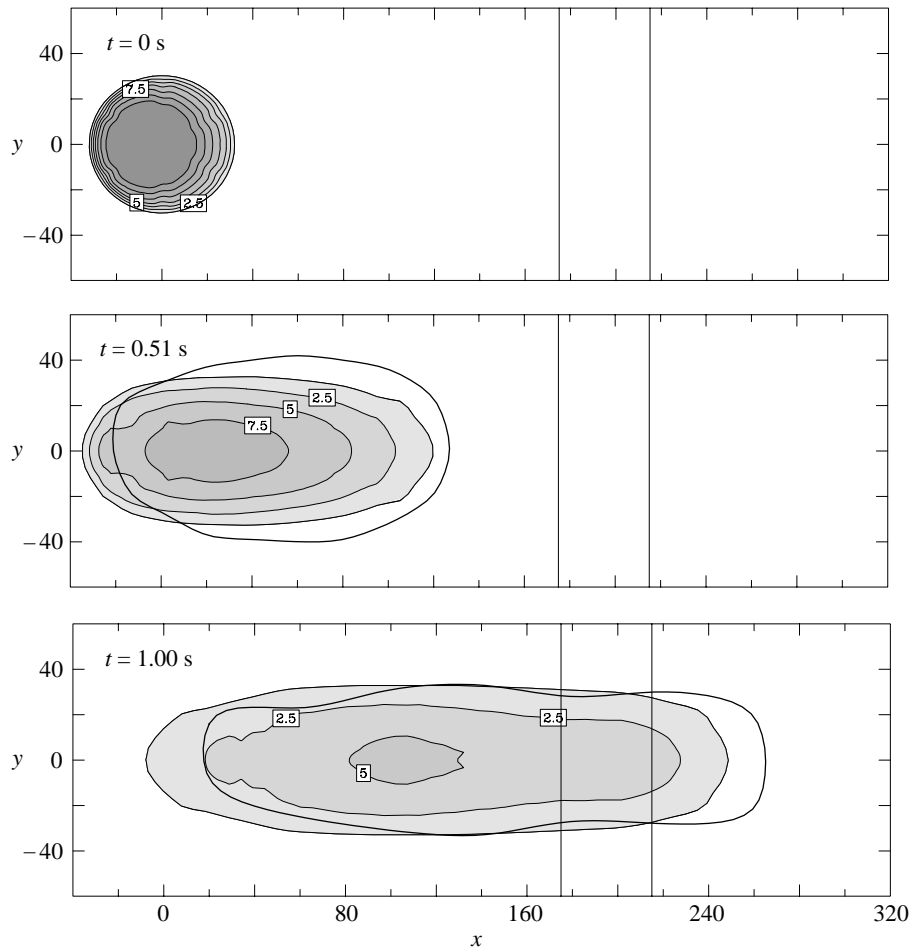
Figure 5. The computed avalanche thickness using the modified basal angle of friction (8.1)
and a comparison with the experimental avalanche boundary (V02).

the downslope direction, as does the granular material on the inclined section of
the chute. However, in the transition zone the motion is dominated by downslope
convergence as the gravitational driving force is reduced to zero here and the material
behind catches up. In the cross-slope direction, the basal topography gradients begin
to dominate in the parabolic section, compressing the *tail* laterally. While in the run-
out zone, the lateral confinement ceases and the avalanche is free to expand laterally
and the earth pressure coefficients change accordingly.

At 1.51 s the nose of the avalanche has virtually come to rest and the whole
avalanche is in downslope convergence as the remaining material in the tail catches
up and increases in thickness. In addition, since lateral confinement ceases on the run-
out plane there is strong cross-slope divergence throughout most of the avalanche,
with only the tip of the tail being compressed. As the avalanche comes to rest at
1.79 s, the velocity and velocity gradients become very small and hence the earth
pressure coefficients become very sensitive to rounding errors.
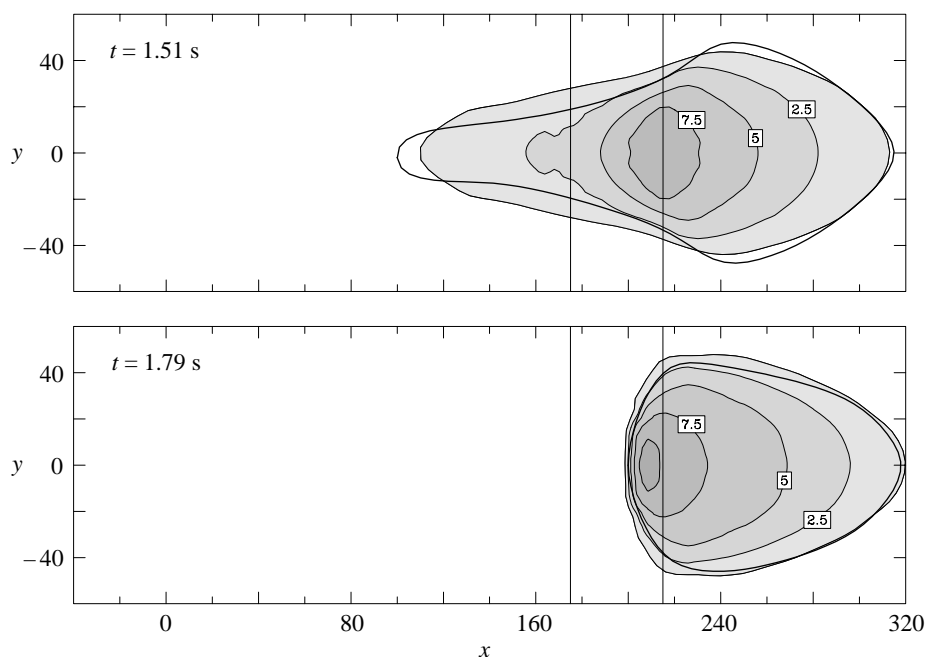
Figure 5. (*Cont.*)

A technical measurement camera (TMK 21), belonging to the Institute of Photogrammetry at the Technische Universität Darmstadt, has been used to take a pair of stereo images of the avalanche deposit. The two pictures, which were taken with a basis of approximately 1.2 m, are shown in figure 8 and give an excellent impression of the avalanche height when viewed through a stereoscope. An AC3 analytical stereo-evaluation device, belonging to the Institute of Photogrammetry, has been used to determine the free surface of the avalanche deposit in experiment V02. A contour plot of the experimental avalanche thickness is illustrated in figure 9, and serves as a further test of the theoretical model. Although the computed avalanche boundary in figure 5 is in very good agreement with that in the experiment, a comparison indicates that the experimental position of maximum thickness is nearly 32 cm further downslope. The contour lines are correspondingly displaced and show that the numerics predict a considerably steeper slope at the back of the avalanche.

9. Comparison with unconfined flow

The partial confinement of an avalanche has a very strong effect on the overall deformation and thickness of the avalanche when in reaches the run-out zone. Of particular significance to civil engineers is the fact that the maximum run-out distance can be significantly enhanced by the channelling effect of a valley. To demonstrate this the results of the previous section are compared with the flow of a similar avalanche on an unconfined chute.

In the following numerical experiment the Mohr–Coulomb model with bed-friction angle reduction (8.1) is used. The simulations are performed with the same parameters as before, except that the parabolic cross-slope profile is removed by letting its
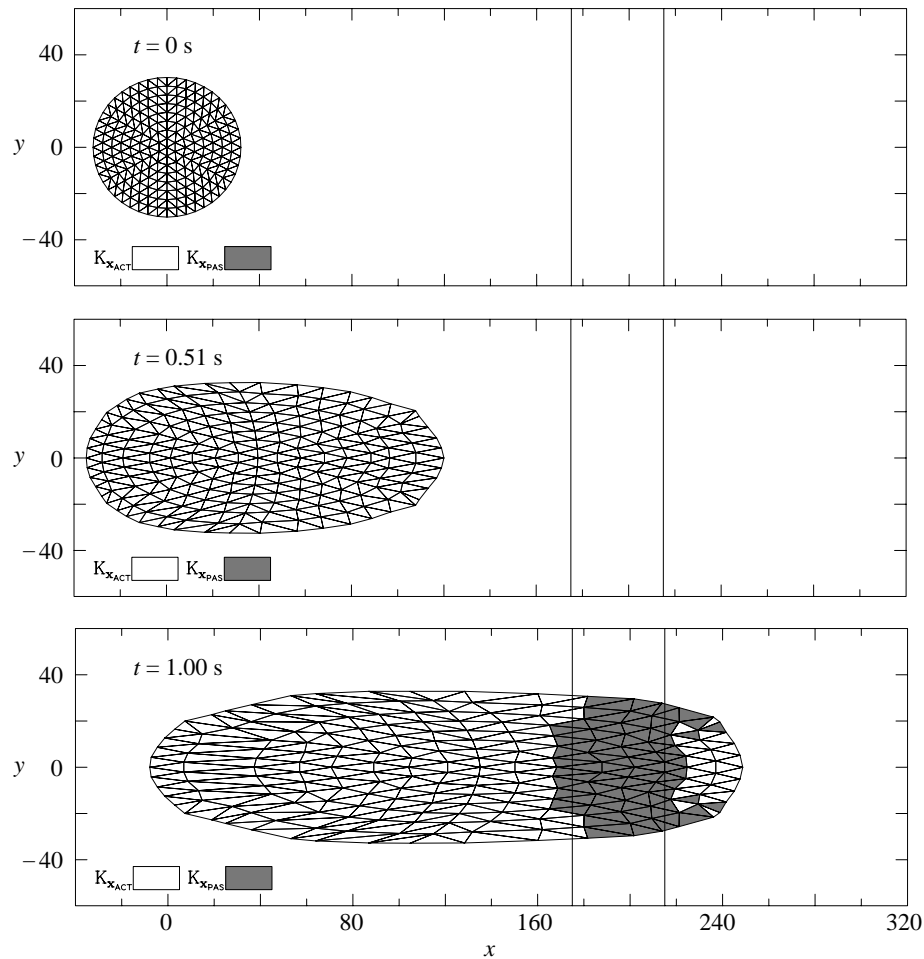
Figure 6. The value of the downslope earth pressure coefficient is illustrated at the same times as in figure 5 by shading the grid cells used in the Lagrangian finite-difference scheme.

radius of curvature $R \to \infty$. A slightly larger volume of granular material is therefore released as the initial configuration is fitted to the flat plane instead of the parabolic chute.

   The predicted avalanche thickness and cross-slope stress state on the unconfined chute are shown in figures 10 and 11, respectively. While the corresponding fields on the partly confined chute are shown in figures 5 and 7. At $t = 0.51$ s the unconfined avalanche spreads out more in both downslope and cross-slope directions. The avalanche length in the downslope direction is almost the same as in the partly confined case, but the width is considerably larger as there are no basal topography gradients to resist the cross-slope spreading. In response to this deformation the $K_{y_{\mathrm{act}}}^{x_{\mathrm{act}}}$ states remain activated throughout the motion on the inclined section of the chute. This contrasts with the partly confined case where there is a slow transition to lateral compression as the basal topography gradients dominate.

   In unconfined flow the thickness and the thickness gradients reduce much more
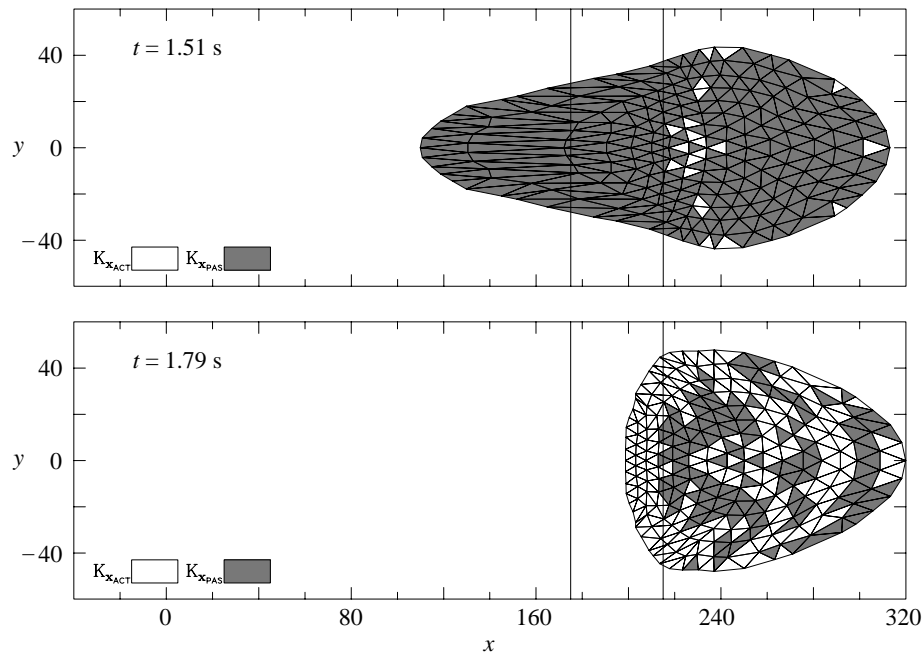
Figure 6. (*Cont.*)

rapidly than in confined flow. The downslope spreading due to the earth pressure terms reduces correspondingly with the result that the avalanche is 10 cm shorter than before after 1 s has elapsed. The downslope stress state is similar to confined flow with a region of convergence in the transition zone followed by diverging motion on the run-out plane. However, only two cross-slope earth pressure states are activated, indicating that the avalanche is always diverging laterally, while in confined flow all four cross-slope earth pressure states are activated. The basal topography gradients are therefore able to induce more complicated material response than on a plane or only longitudinally curved surface.

The unconfined avalanche does not develop the tadpole-like shape observed during partly confined flow after 1.51 s. The downslope convergence increases the thickness of the avalanche, but despite the larger initial volume the maximum thickness is 2–3 cm smaller than before. The unconfined avalanche also comes to rest at approximately 1.79 s. However, the boundary of the avalanche is considerably different in shape. The maximum run-out distance is 20 cm shorter on the unconfined chute than on the partly confined chute, which is significant as it implies that the basal topography strongly effects the maximum avalanche run-out distance. It is also important to note that the unconfined avalanche spreads 30 cm further out on either side of the confined chute boundary.

The one-dimensional Savage–Hutter model is being used increasingly by civil engineers to map the risk of snow avalanches in populated mountainous regions. The aim being to limit or prevent further development in high-risk zones. The two-dimensional simulations performed here show that the basal topography can have a significant effect on both the maximum run-out distance and the run-out width. On the laboratory scale these differences are of the order of tens of centimetres, but on the
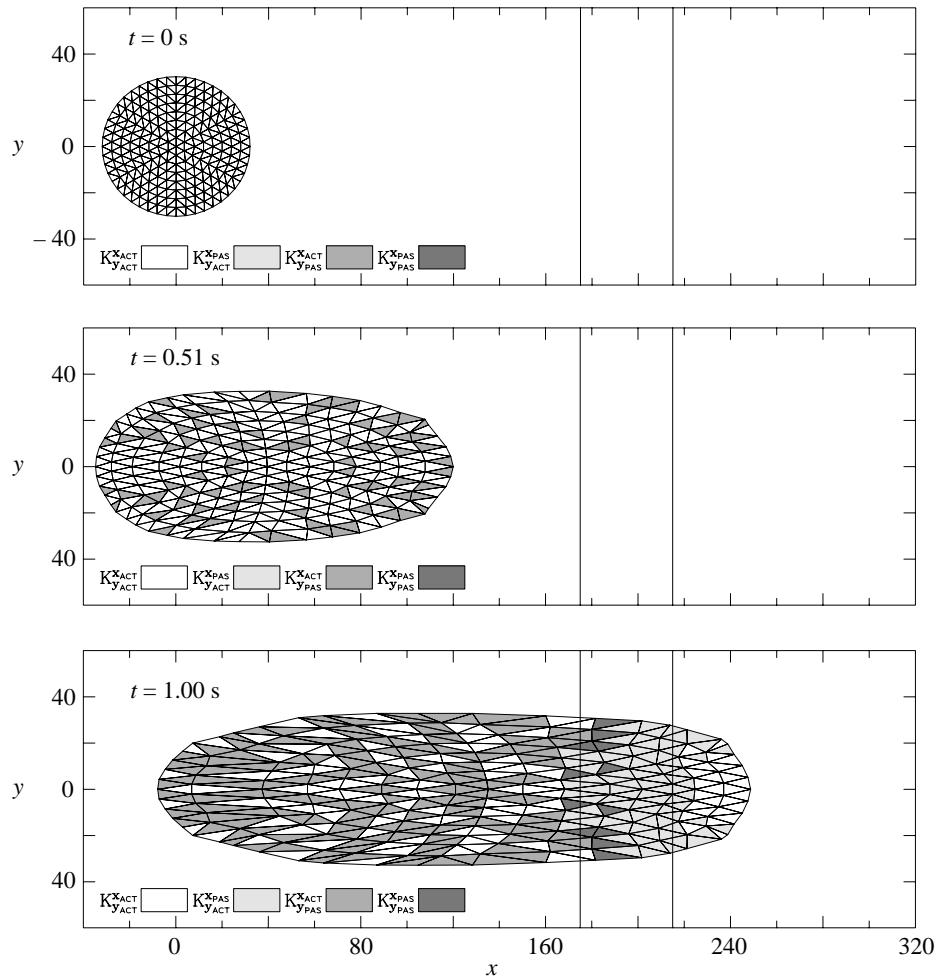
Figure 7. The cross-slope earth pressure coefficients are illustrated by shading the grid cells used in the numerical finite-difference scheme.

environmental scale, where the channelled valley may be 2 km long, these differences will be of the order of several hundred metres, which are significant.

10. Shallow-water avalanche model (SWAM)

The system of partial differential equations (7.14), (7.18) and (7.19) for the avalanche thickness and velocity are very similar in form to the shallow-water equations of fluid dynamics. The theory differs naturally in respect to the coordinate system, the nature of the forcing terms and the drag relations; however, the only major difference lies in the assumed constitutive properties. One-dimensional hydraulic avalanche models of this kind were first put forward by Eglit (1983), but no numerical solutions have been performed in either one or two dimensions. It is therefore of considerable interest to determine how well the shallow-water equations can describe the flow of granular avalanches over complex topography.
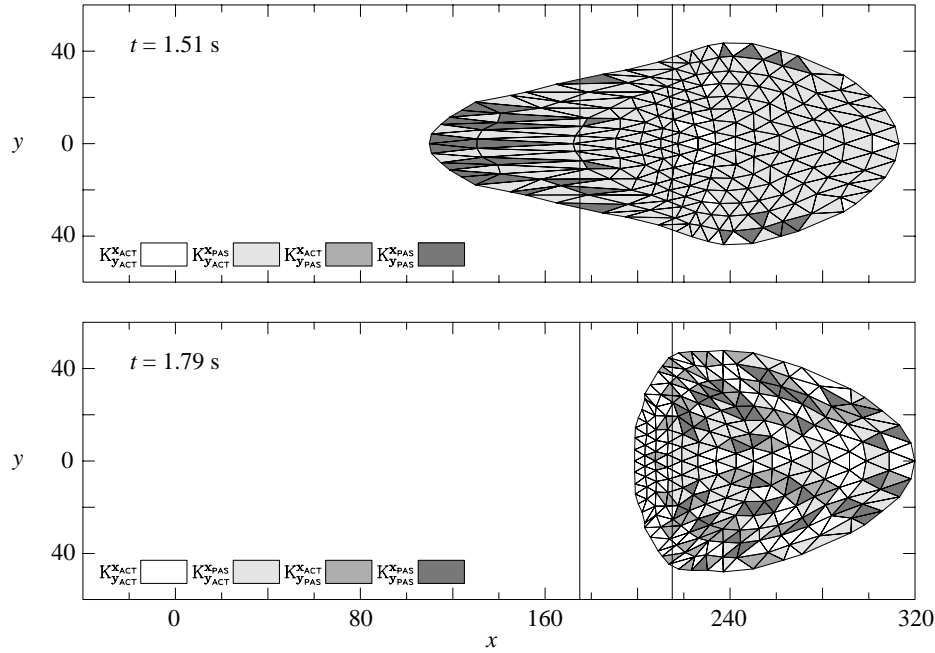
Figure 7. (*Cont.*)

The SWAM provides an alternative closure scheme to the Mohr–Coulomb model with simpler constitutive properties. It is assumed that the stress is isotropic, i.e.

$$p_{xx} = p_{yy} = p_{zz}, \tag{10.1}$$

and that the normal pressure p_{zz} is given by (6.10). It follows that the stress ratios remain constant throughout the deformation and that the analogous earth pressure coefficients for the shallow-water model are

$$K_x = 1, \quad K_y = 1. \tag{10.2}$$

A two-dimensional SWAM can therefore be constructed by replacing the earth pressure coefficients defined in (7.3)–(7.6) by the simpler relations (10.2). In the Mohr–Coulomb model the internal angle of friction $\phi = 40°$ and the basal angle of friction at the front of the avalanche $\delta_0 = 30°$. It follows that for these values the earth pressures coefficients $K_{x_{\mathrm{act}}} = 0.81$ and $K_{y_{\mathrm{act}}}^{x_{\mathrm{act}}} = 0.325$, which are both less than unity. This implies that for the same thickness gradients the spreading force of the earth pressure terms is significantly lower in the Mohr–Coulomb model than in the SWAM. However, during downslope convergence, $K_{x_{\mathrm{pas}}}$ is larger than unity, which implies that greater thickness gradients can be sustained.

The computed thickness distributions using the SWAM with bed-friction angle reduction (8.1) on the partly confined chute are illustrated in figure 12. At $t = 0.51$ s the SWAM has spread out slightly further in the downslope direction and much further in the cross-slope direction, so that the avalanche is thinner than in figure 5. The agreement with the experimentally determined avalanche boundary is at least as good as that obtained with the Mohr–Coulomb model.

The SWAM is still slightly thinner and more spread out than the Mohr–Coulomb model after 1 s and both models agree equally well on the position of the experi-
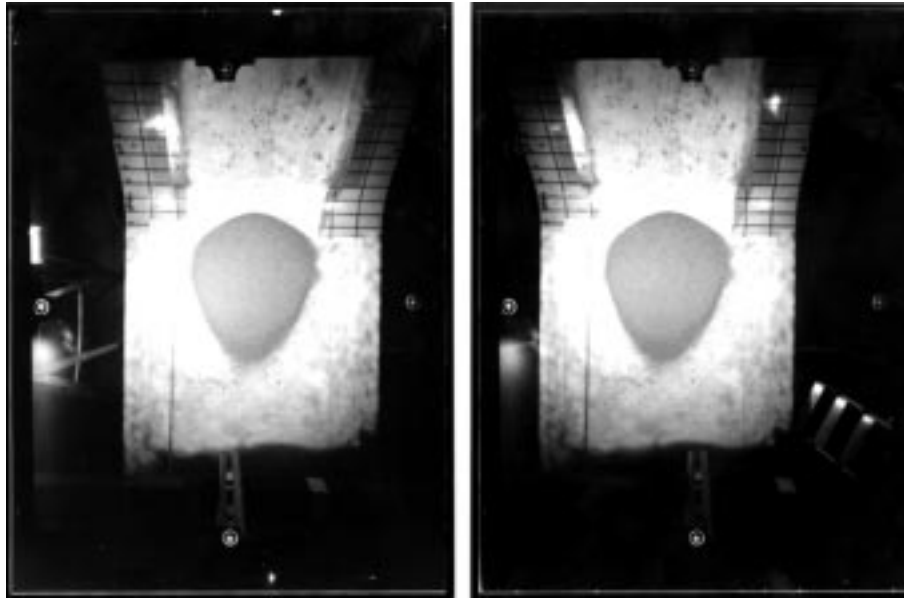
Figure 8. An image pair of the avalanche deposit taken with the Technical Measurement Camera (TMK 21).
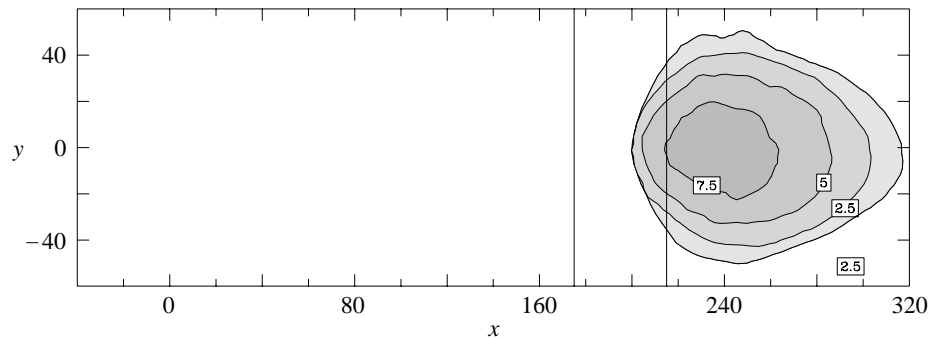

Figure 9. The final thickness distribution of experiment V02 is determined from the stereo images by photogrammetric techniques. It is illustrated here in projected curvilinear coordinates (x, y) and contour intervals in centimetres.

mentally determined boundary. In the tail section of the avalanche, the predominant cross-slope earth pressure coefficient $K^{x_{\mathrm{act}}}_{y_{\mathrm{pas}}} = 1.49$ in the Mohr–Coulomb model, which in lateral convergence provides more resistance to compression than in the SWAM where $K_y = 1$. It follows that in the Mohr–Coulomb model the channelling effect of the basal topography gradients is almost in balance with the cross-slope spreading, while in the SWAM, where there is not as much resistance to compression, the lateral topography gradients cause a strong compression of the flow. In the transition zone the SWAM is still converging laterally, while in the Mohr–Coulomb model there is lateral divergence.

Large differences appear between the two models as the body of the avalanche passes the transition zone and enters the run-out plane. Here downslope conver-
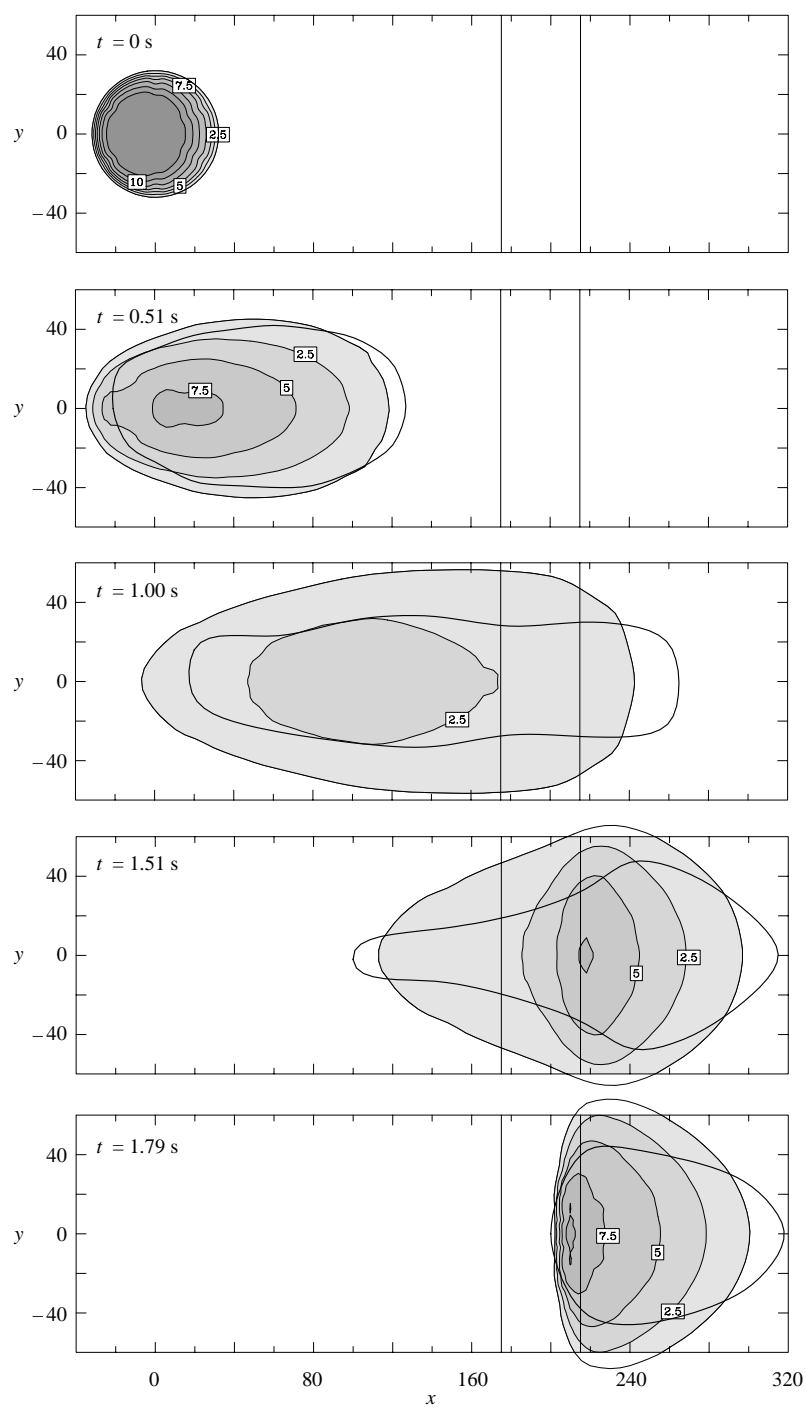
Figure 10. The computed avalanche thickness on a chute without lateral confinement is illustrated at a sequence of time-steps. The thick solid line shows a comparison with experiment (V02).
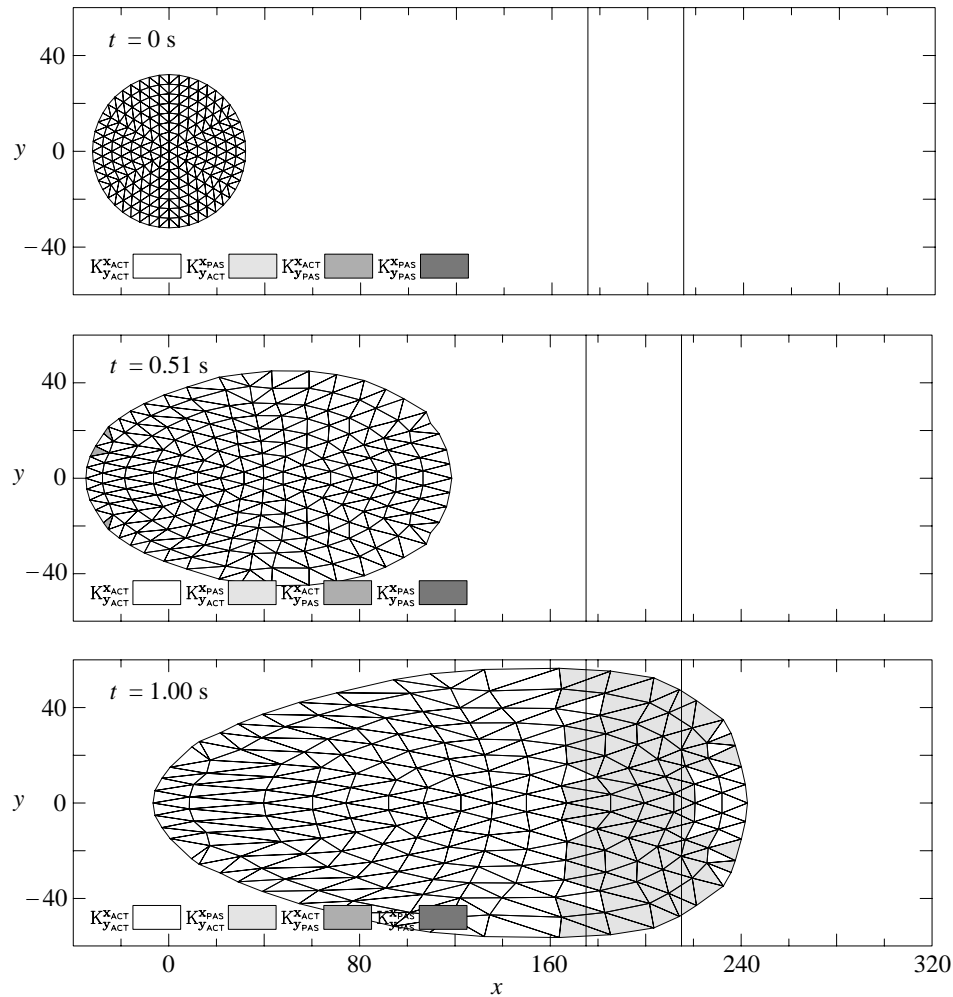
Figure 11. The cross-slope earth pressure coefficients on the unconfined chute are illustrated by shading the grid cells used in the numerical finite-difference scheme.

gence dominates and the lower downslope earth pressure coefficient in the SWAM allows larger thickness gradients to be sustained before the nose of the avalanche can advance forward into the run-out zone. However, the avalanche spreads out strongly in the lateral direction due to the larger cross-slope earth pressure in the SWAM in unconfined lateral divergence. The large thickness gradients delay the arrival of the avalanche tail, which is still moving down through the transition zone when the experimental avalanche comes to rest at 1.79 s.

The shape of the avalanche deposit in the transition zone is completely different from that of the Mohr–Coulomb model. A comparison with the boundary of the experimental avalanche shows that the SWAM seriously underpredicts the maximum run-out distance, which is of crucial importance in avalanche prediction. While the Mohr–Coulomb model is not perfect, these results demonstrate that the variation of the earth pressure coefficients in (7.3)–(7.6) is at least qualitatively correct.
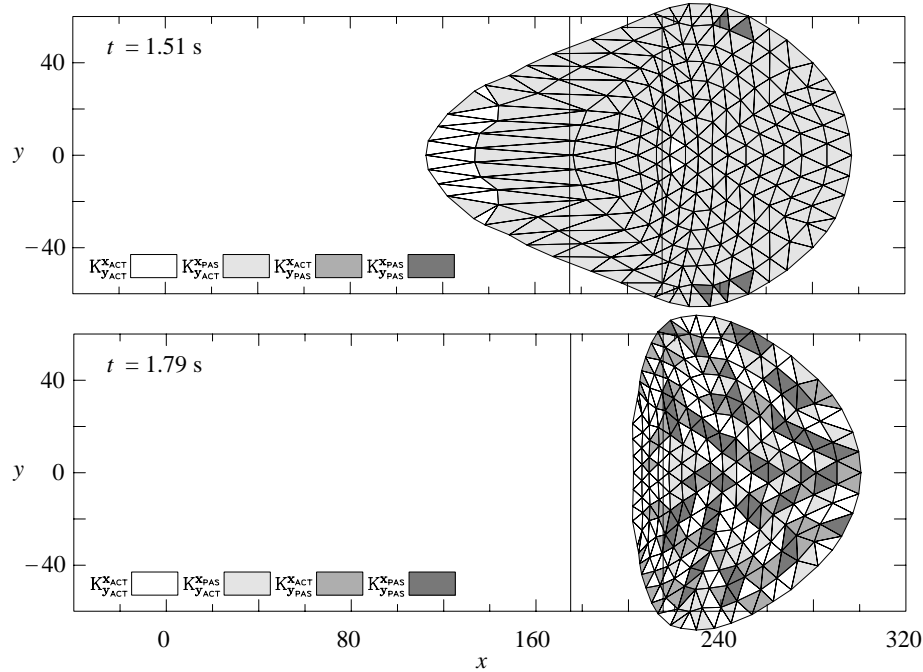
Figure 11. (*Cont.*)

11. Discussion

The Savage–Hutter theory has been extended in this paper to model the flow of granular avalanches over complex three-dimensional basal topography. This has been achieved by using an orthogonal curvilinear coordinate system, which follows the 'mean' topography of the slope, and superposing shallow three-dimensional topography above this *reference* surface. The resulting depth-integrated two-dimensional theory is capable of predicting the flow of granular avalanches over realistic topographic features. It is therefore envisaged that this model will find important application in assessing avalanche, landslide and rock fall hazards in populated mountainous regions, where *terrain specific* information is vital to accurately predict maximum run-out distances.

The laboratory experiment (V02) on the partly confined chute is in good agreement with theoretical predictions (figure 4), although the computed avalanche tail moves too slowly. The cause of this is almost certainly because the Coulomb sliding law with a constant bed-friction angle is unrealistic. As the avalanche accelerates, the apparent friction angle will dynamically evolve from the static to dynamic states, and rate dependent Voellmy drags at both the surface and base of the avalanche may become important. In addition, at very high rates the basal boundary may induce large granular temperatures that fluidize the flow and reduce the basal friction. The correct friction law is still an open question, but it has been shown here that experiment and theory can be brought into excellent agreement by a simple reduction of the friction angle in the tail of the avalanche (figure 5). Further experiments are necessary, however, to understand the basic physics of the frictional processes taking place at the base of the avalanche.
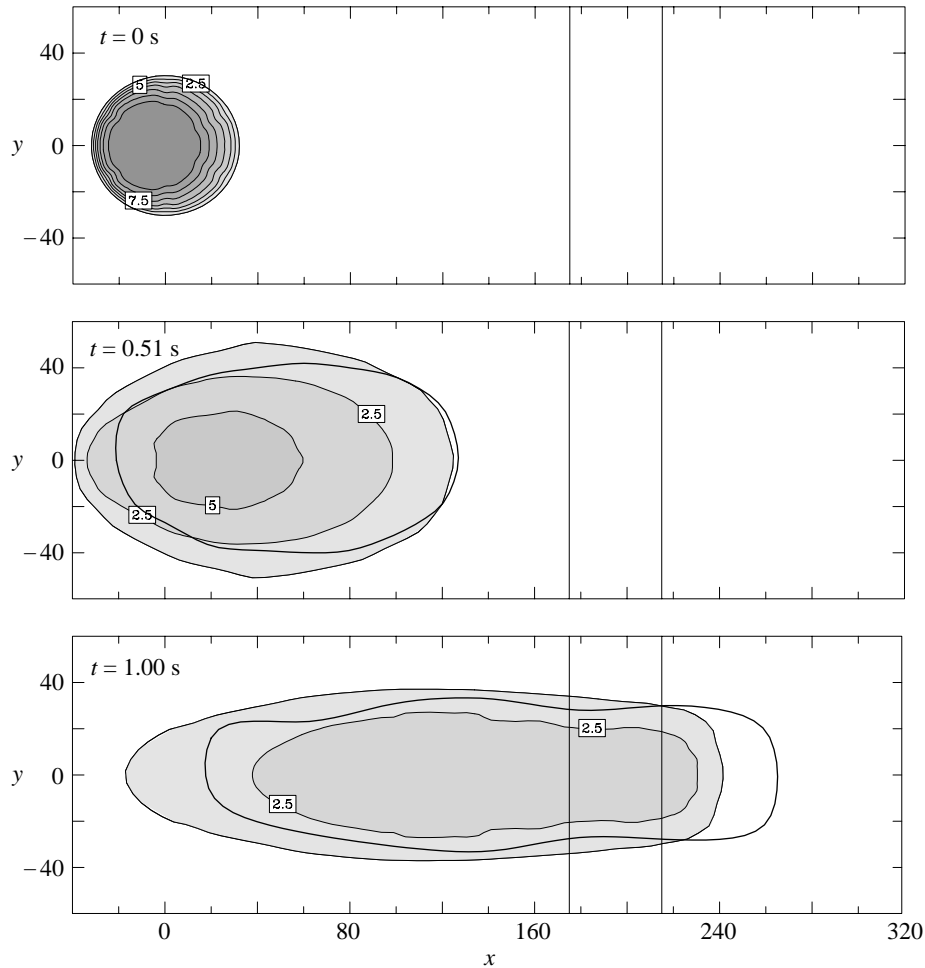
Figure 12. The computed avalanche thickness using the SWAM is illustrated at a sequence of time-steps. The thick solid line shows a comparison with experiment (V02).

The partly confined chute prevents lateral expansion and channels the flow. As a result, the maximum run-out distances are significantly longer than on an unconfined chute (figure 10), although the unconfined avalanche spreads out far wider. These observations demonstrate the importance of the topographic effect on avalanche flow and the final position of the deposit. The spreading of the avalanche is also significantly influenced by the assumed constitutive properties, as the SWAM shows. While the avalanche is in divergence this hydraulic model is in good agreement with the experiment (V02). However, as soon as the avalanche begins to converge in the run-out zone the reduced value of the earth pressure coefficients results in a much more compact deposit (figure 12), and the maximum run-out distance is underpredicted. This demonstrates that the variation of the earth pressure coefficients with the Mohr–Coulomb model is at least qualitatively correct.
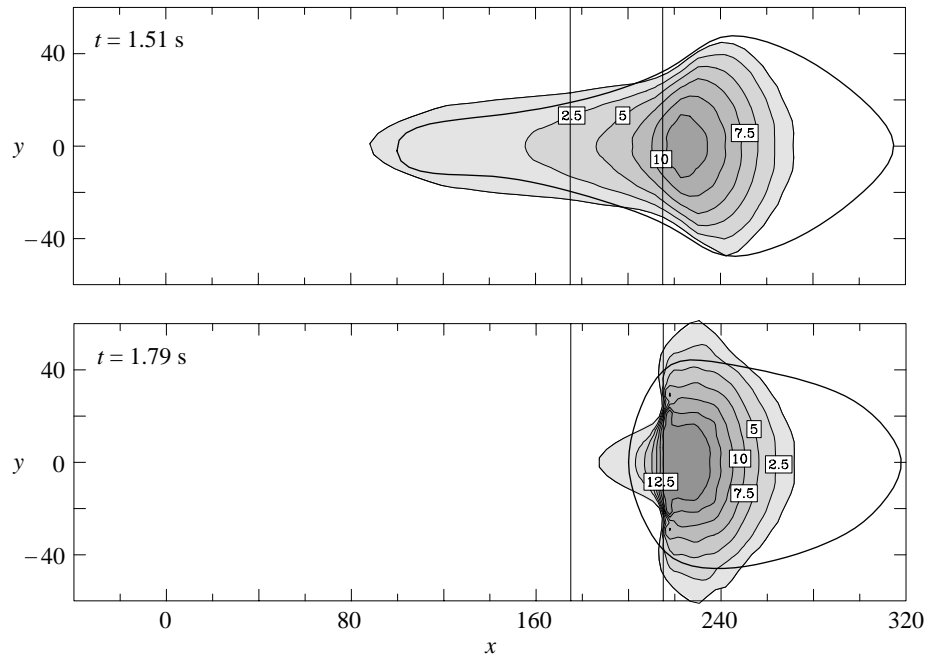
Figure 12. (*Cont.*)

References

Brillouin, L. 1964 *Tensors in mechanics and elasticity*. New York: Academic.

Dent, J. D., Burrel, K. J., Schmidt, D. S., Louge, M. Y., Adams, E. E. & Jazbutis, T. G. 1998 Density, velocity and friction measurements in a dry-snow avalanche. *Annal. Glac.* **26**, 247–252.

Eglit, M. E. 1983 Some mathematical models of snow avalanches. In *Advances in mechanics and the flow of granular materials* (ed. M. Shahinpoor), vol. 2, pp. 577–588. Houston, TX: Clausthal–Zellerfeld and Gulf Publishing Company.

Greve, R. & Hutter, K. 1993 Motion of a granular avalanche in a convex and concave curved chute: experiments and theoretical predictions. *Phil. Trans. R. Soc. Lond.* A **342**, 573–600.

Greve, R., Koch, T. & Hutter, K. 1994 Unconfined flow of granular avalanches along a partly curved surface. I. Theory. *Proc. R. Soc. Lond.* A **445**, 399–413.

Hungr, O. & Morgenstern, N. R. 1984*a* Experiments on the flow behaviour of granular materials at high velocity in an open channel flow. *Geotechnique* **34**, 405–413.

Hungr, O. & Morgenstern, N. R. 1984*b* High velocity ring shear tests on sand. *Geotechnique* **34**, 415–421.

Hutter, K. & Koch, T. 1991 Motion of a granular avalanche in an exponentially curved chute: experiments and theoretical predictions. *Phil. Trans. R. Soc. Lond.* A **334**, 93–138.

Hutter, K., Siegel, M., Savage, S. B. & Nohguchi, Y. 1993 Two-dimensional spreading of a granular avalanche down an inclined plane. I. Theory. *Acta Mech.* **100**, 37–68.

Hutter, K., Koch, T., Plüss, C. & Savage, S. B. 1995 The dynamics of avalanches of granular materials from initiation to run-out. *Acta Mech.* **109**, 127–165.

Keller, S., Ito, Y. & Nishimura, K. 1998 Measurements of the vertical velocity distribution in ping pong ball avalanches. *Annal. Glac.* **26**, 259–264.

Klingbeil, E. 1966 Tensorrechnung für ingenieure. Bibliographisches Institut, Mannheim: Hochschultaschenbücher.

Koch, T., Greve, R. & Hutter, K. 1994 Unconfined flow of granular avalanches along a partly curved chute. II. Experiments and numerical computations. *Proc. R. Soc. Lond.* A **445**, 415–435.

McConnell, A. J. 1957 *Applications of tensor analysis.* New York: Dover.

Savage, S. B. & Hutter, K. 1989 The motion of a finite mass of granular material down a rough incline. *J. Fluid Mech.* **199**, 177–215.

Savage, S. B. & Hutter, K. 1991 The dynamics of avalanches of granular materials from initiation to run-out. I. Analysis. *Acta Mech.* **86**, 201–223.

Sokolnikoff, I. S. 1951 *Tensor analysis theory and applications.* New York: Wiley.